



**CHALMERS**  
UNIVERSITY OF TECHNOLOGY

## **Decoding the Structure of Benzodithiophene Polymers for High-Efficiency Organic Solar Cells**

Downloaded from: <https://research.chalmers.se>, 2026-05-14 12:49 UTC

Citation for the original published paper (version of record):

Sanviti, M., Marina, S., Rodriguez-Martínez, X. et al (2025). Decoding the Structure of Benzodithiophene Polymers for High-Efficiency Organic Solar Cells. *Advanced Functional Materials*, 35(44). <http://dx.doi.org/10.1002/adfm.202503634>

N.B. When citing this work, cite the original published paper.

# Decoding the Structure of Benzodithiophene Polymers for High-Efficiency Organic Solar Cells

Matteo Sanviti, Sara Marina, Xabier Rodriguez-Martínez, Jesika Asatryan, Valerio Di Lisio, Sandra Hultmark, Junkal Gutierrez, Eduardo Solano, Jeromy J. Rech, Eugenio L. Solla, Wei You, Agnieszka Tercjak, M. Eugenio Vázquez, Daniele Cangialosi, Christian Müller, Harald Ade, and Jaime Martin\*

The performance of organic electronic devices, such as solar cells, depends on understanding and controlling the solid-state microstructure of semiconducting polymers. In this study, a detailed understanding of the aggregate states, solid-state microstructure, and thermotropic behavior of the best-performing family of polymers for solar cells, i.e., benzodithiophene-based semiconducting polymers, is provided. Using D18, PBnDT-FTAZ, and PBDB-T-Cl as model systems, this study reveals a unique solid mesophase, distinct from previously observed polymer mesophases, comprising stacked solid-like and liquid-like layers. This mesophase resembles smectic structures while also sharing features with columnar mesophases like condensation crystals and paracrystals. At a larger length scale, it organizes into nanoscale fibril-like domains, with polymer backbones aligned along the fibril axis, coexisting with amorphous-like glassy regions, reported here for the first time. Notably, high-performance polymers such as D18, D18-Cl, and PM6 contain minimal glassy regions. The thermotropic behavior of this biphasic nanomorphology is also examined, providing insights into how thermal annealing influences polymer structure. Understanding these solid-aggregate states, the microstructure, and the thermal behavior enables a more precise framework for defining structure–function relationships in semiconducting polymers. This will have a significant impact on the entire field of organic electronics, from organic photovoltaics to bioelectronics to wearable electronics.

## 1. Introduction

The field of organic electronics is experiencing rapid growth due to the numerous advantages offered by organic semiconductors and in particular semiconducting polymers. These advantages include flexibility, semitransparency, chemical tunability, ease of processing, and low fabrication costs. The operation of the majority of organic electronic devices is contingent upon physical processes that are inextricably linked to the solid-state microstructure of the polymer materials from which they are constructed (e.g., charge carrier transport, exciton recombination dynamics, etc.).<sup>[1]</sup> This is to say that the packing of polymer molecules in space is a fundamental determinant of device performance. Consequently, the rational optimization of the majority of devices stems from the understanding of, and subsequent manipulation of, the solid-state microstructure of semiconducting polymers. To achieve this, the microstructure of semiconducting polymers was initially rationalized according to the classical structural models of

M. Sanviti, X. Rodriguez-Martínez, J. Asatryan, J. Martin  
Campus Industrial de Ferrol  
Universidade da Coruña  
CITENI, Campus de Esteiro S/N, Ferrol 15471, Spain  
E-mail: [jaime.martin.perez@udc.es](mailto:jaime.martin.perez@udc.es)

 The ORCID identification number(s) for the author(s) of this article can be found under <https://doi.org/10.1002/adfm.202503634>

© 2025 The Author(s). Advanced Functional Materials published by Wiley-VCH GmbH. This is an open access article under the terms of the [Creative Commons Attribution-NonCommercial-NoDerivs License](#), which permits use and distribution in any medium, provided the original work is properly cited, the use is non-commercial and no modifications or adaptations are made.

DOI: 10.1002/adfm.202503634

S. Marina  
POLYMAT  
University of the Basque Country  
UPV/EHU Av. de Tolosa 72, Donostia-San Sebastián 20018, Spain  
V. Di Lisio, D. Cangialosi  
Donostia International Physics Center  
Paseo Manuel de Lardizabal 4, San Sebastián 20018, Spain  
S. Hultmark, C. Müller  
Department of Chemistry and Chemical Engineering  
Chalmers University of Technology  
Göteborg 41296, Sweden  
J. Gutierrez, A. Tercjak  
Group 'Materials + Technologies', Faculty of Engineering Guipuzcoa  
University of the Basque Country (UPV/EHU)  
Plaza Europa 1, Donostia 20018, Spain

polymers, i.e., the amorphous and the semicrystalline models.<sup>[1,2]</sup> However, these traditional models, which were developed for simpler polymers, have consistently failed to accurately depict the microstructure of many if not most semiconducting polymers.<sup>[3]</sup> More recently, other more complex forms of molecular organizations have also been proposed, such as liquid crystals, condensation crystals, etc., as will be discussed later.<sup>[1,3,4]</sup>

Many of the most effective donor polymers for organic photovoltaics (OPV), e.g., the polymers commonly abbreviated as D18, PBDB-T, PM6, or PBnDT-FTAZ (and their derivatives), possess backbones that include a substituted benzodithiophene unit (see Figure 1a–c). In the case of these polymers, the benzodithiophene units are combined with other building blocks and moderately large fractions of mostly aliphatic side chains. When cast into thin films, as it is typically the case of OPV devices, they often exhibit grazing incidence wide-angle X-ray scattering (GIWAXS) patterns with a few and broad peaks. Figure 1d–f shows representative GIWAXS patterns for spun cast PBnDT-FTAZ, PBCB-T-Cl, and D18, respectively. These GIWAXS patterns are dominated by reflections resulting from a periodic alternation of backbones and side chains, commonly referred to as (*h*00) peaks, and reflections from the lateral packing of backbones, frequently in an orthogonal direction to the former, which are typically designated as (0*k*0) peaks. The (*h*00) and (0*k*0) peaks often manifest along the meridian (i.e., the *z*-axis) and the equator (i.e., the *x*- and *y*-axes) of the GIWAXS patterns (for details, see the experimental geometry in Figure S1a, Supporting Information). Furthermore, some polymers, including PBCB-T-Cl and D18, also feature a (00*l*) series of peaks that are associated with spatial correlations along the aromatic backbones.<sup>[5]</sup> The lack of mixed-index peaks indicates the absence of 3D structural order. It must be noted

that all the diffraction features mentioned above frequently show up in GIWAXS patterns of polymer:nonfullerene–acceptor (polymer:NFA) blend films used as active layers in OPV devices (see Figure 1b, Supporting Information).

The (100) peak can be remarkably intense, yet broad, often reflecting coherence lengths of only a few nanometers.<sup>[2c,3]</sup> However, the presence of periodically spaced higher-order peaks is often observed, collectively indicating the existence of long-range lamellar order in that direction, which has been furthermore confirmed by electron microscopy.<sup>[6]</sup> The lamellar structure in semiconducting polymers is a consequence of their intrinsic chemical asymmetry, namely, the different chemical nature of the backbones and side chains. The backbones and side chains of semiconducting polymers can be mutually immiscible, and they also display different molecular conformations and mobilities, which together result in nanoscale self-assembled domains with high concentrations of backbones or side chains.

The (010) peaks in benzodithiophene-based polymers tend to be broader than typical Bragg peaks of semicrystalline polymers. Coherence lengths of 1–2 nm are often measured for (0*k*0) peaks,<sup>[3]</sup> which indicate limited long-range positional order in the backbones' packing along this direction. However, (010) peaks are observed to be more intense and better defined than typical diffuse scattering peaks of regular amorphous polymers, i.e., the so-called “amorphous halos,” suggesting that a certain degree of order may exist in the lateral packing of polymer chains. Moreover, because no independent “amorphous halo” from backbones is typically documented (e.g., akin to that of amorphous regions of semicrystalline polymers), it can be surmised that the (010) peak is indicative of the overall packing of backbones in directions other than that of the lamellar periodicity. This may encompass both  $\pi$ -stacked chain segments and other chain segments that are more disorderly packed. It should be noted that some materials feature an “amorphous halo” that be attributed to the amorphous packing of side chains.<sup>[7]</sup>

It is evident that the GIWAXS patterns of benzodithiophene-based polymers described above are different from those of amorphous and semicrystalline polymers. Consequently, the solid aggregate state(s) in which these polymers organize must differ from the isotropically disordered ensemble of random coils of amorphous polymers and the lamellar crystals of semicrystalline polymers. This is the reason why traditional structural models are not generally applicable to semiconducting polymers employed in OPV. Alternatively, their structure may be situated within a generic and often poorly defined group of polymeric low-order aggregate states, i.e., solid mesophases,<sup>[8]</sup> whose structural order is characterized by an intermediate state between that of the ordered crystalline phase and the isotropic liquid/glass. These include, for example, hexagonal phases,<sup>[9]</sup> (micro)paracrystals,<sup>[10]</sup> vitrified liquid crystals,<sup>[11]</sup> conformationally disordered (condensation) crystals,<sup>[12]</sup> and columnar phases<sup>[13]</sup> (see schematic illustrations of the mesophases in Figure 1g–j). It is important to note that some of the aforementioned mesophases, such as hexagonal phases, columnar phases, and condensation crystals, frequently refer to highly similar—if not the same—structures, as will be discussed below.

Vitrified liquid crystals form when a liquid-crystalline mesophase undergoes vitrification, e.g., by rapid cooling the material below the glass transition temperature,  $T_g$ . The

J. Gutierrez  
Faculty of Engineering Vitoria-Gasteiz  
University of the Basque Country (UPV/EHU)  
C/Nieves Cano 12, Vitoria-Gasteiz 01006, Spain

E. Solano  
NCD-SWEET beamline  
ALBA Synchrotron Light Source  
Cerdanyola del Vallès 08290, Spain

J. J. Rech, W. You  
Department of Chemistry  
University of North Carolina at Chapel Hill  
Chapel Hill, NC 27599, USA

E. L. Solla  
Servicios de apoyo a la investigación (SAI)  
Universidade da Coruña  
Campus de Elviña, s/n, A Coruña 15071, Spain

M. E. Vázquez  
Centro Singular de Investigación en Química Biolóxica e Materiais Moleculares (CiQUS)  
Departamento de Química Orgánica  
Universidade de Santiago de Compostela  
Santiago de Compostela 15705, Spain

D. Cangialosi  
Centro de Física de Materiales  
(CSIC-UPV/EHU) Paseo Manuel de Lardizabal 5, Sebastián 20018, Spain  
H. Ade  
Department of Physics and Organic and Carbon Electronics Laboratories (ORaCEL)  
North Carolina State University  
Raleigh, NC 27695, USA

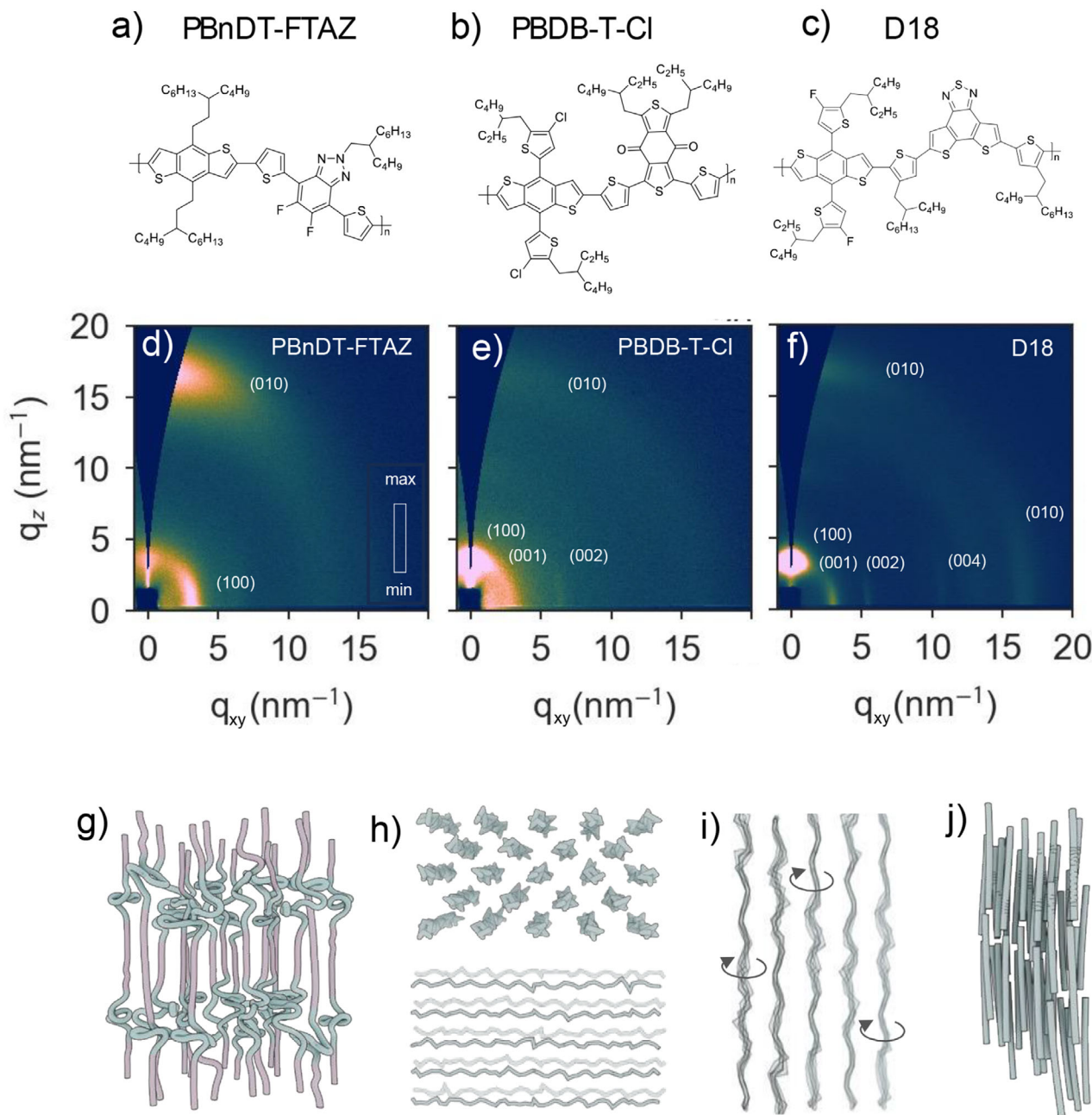


**Figure 1.** a) Chemical structures of PBnDT-FTAZ, PBDB-T-Cl, and D18. b) Representative 2D-GIWAXS patterns of spun cast PBnDT-FTAZ and PBDB-T-Cl and D18 thin films. c) Schematics of solid mesophases found in polymer materials: g) vitrified (smectic) liquid crystal, h) hexagonal and columnar phase, i) condisc crystal, and j) paracrystal.

thus formed solid mesophase retains the molecular order (orientational, positional, etc.) of the precursor liquid-crystalline mesophase (Figure 1g).<sup>[4b,14]</sup> Likewise, vitrified liquid crystals must devitrify into the liquid-crystalline mesophase when they are heated above the  $T_g$ . Typical polymers that exhibit liquid-crystalline phases feature rigid-rod, disk-like or board-like mesogens and/or amphiphilic character, which are conditions that benzodithiophene-based polymers fulfill.

Hexagonal phases are characterized by rather disordered hexagonal-like stacks of chains that point in the same direc-

tion (Figure 1h).<sup>[9]</sup> They exhibit orientational order but lack of long-range positional order along the chain direction. Therefore, hexagonal phases exhibit solely 2D positional order. They must be differentiated from smectic B phases, as hexagonal phases do not feature density fluctuations resulting in lamellar-like order. Because chains in hexagonal phases resemble columnar structures, these mesophases are also referred to as columnar phases.<sup>[13b]</sup>

Condisc crystals refer to a similar structure formed by aligned chains. They exhibit long range positional order in directions

perpendicular to chains but lack of positional order in the chain direction.<sup>[12b,14,15]</sup> The chain arrangement in condis crystals frequently features hexagonal order although, in principle, that is not a requisite.<sup>[16]</sup> The main conceptual difference with hexagonal and columnar phases is that the lack of positional order along chains in condis crystals results from local cooperative molecular motions, which allow chains to reach distinct conformational isomers (Figure 1i). However, such motions are frozen-in below a certain temperature, which is analogous to a  $T_g$  of the condis crystal. Thus, below that temperature, condis crystals, hexagonal phases, and columnar phases can be often equivalent.

Paracrystallinity is a crystal model characterized by cumulative lattice distortions and hence by limited order along given lattice directions. Thus it is a suitable framework to characterize mesophases' order. Here, long-range correlated lattice distortions are produced by statistically homogeneous disturbances to an ideal crystalline lattice, giving rise to a lattice of partial order, i.e., a mesophase.<sup>[10b,17]</sup> To measure the statistical fluctuations of local arrangement of atoms, i.e., the disorder of the paracrystalline lattice, the paracrystalline distortion parameter,  $g$ , was introduced.  $g$  is the ratio of statistical fluctuations  $\Delta a_{ik}$  of a lattice vector  $a_i$  along the direction  $a_k$ , ( $g_{ik} = \frac{\Delta a_{ik}}{a_k}$ ) hence, it measures the degree of disorder of the lattice. The  $g$ -parameter ranges between 0%, for a distortion-free crystal, to 100%, for a Boltzmann gas. A  $g$ -parameter of 2–4% is typically found in common semicrystalline polymers, while 7–12% are standard  $g$ -values of paracrystalline mesophases.<sup>[10b]</sup> The  $g$ -parameter can be extracted using formalisms that allow to separate the different contributions to the breadth of diffraction peaks, such as the Williamson–Hall<sup>[18]</sup> and the Warren–Averbach<sup>[19]</sup> methods. Hosemann et al. proposed that microparacrystals are the “building bricks” of many types of condensed matter, including some polymer materials.<sup>[17a]</sup> That seems to be especially the case of spun fibers of rigid polymers, such as poly(phenylene terephthalamide (i.e., Kevlar) fibers.<sup>[20]</sup> Within these fibers, rigid-rod-like chains align in the drawing direction and stack laterally, resulting thus in a columnar-like structure with paracrystalline order (Figure 1j). Because no disordered chains are present in these fibers, the entire material can be pictured as an imperfect lattice of stacked chains, i.e., a (micro)paracrystal. Consequently, the  $g$ -parameter suffices to capture the overall degree of structural order in paracrystalline fibers.

It is noteworthy that all the mesophases above mentioned are, to some extent, compatible with the X-ray patterns shown in Figure 1d–f. Therefore, a major question is whether any of these mesophases can explain the nature of the structural order in donor semiconducting polymers for OPV. However, to date, few studies have thoroughly investigated the mesophase in conjugated polymers.<sup>[1,2c,4a,b,c,11a,17b]</sup> Instead, given the low degree of structural order and the reduced size of ordered domains in these materials, these are frequently designated with the generic term “aggregate” or simply “crystals/crystallites.”<sup>[1,21]</sup>

Based on the thermotropic behavior of alkyl-substituted polypeptoids and aromatic polyesters and polyimides.<sup>[11b,22]</sup> Daoulas and co-workers described the structure of conjugated polymers in the frame of sanidic liquid-crystalline mesophases.<sup>[4a,11a]</sup> In common materials featuring sanidic mesophases, structural order develops in different steps, i.e., the development of lamellar order and the crystallization of backbone

chains inside one of the layers. Hence, the order–disorder transition and the solid–liquid transition occur independently (at different temperatures) in sanidic materials. Interestingly, it should be highlighted that the thermotropic behavior of some semiconducting polymers, such as PBTTT, is remarkably similar to that reported for alkyl-substituted aromatic polyesters and polyamides and polypeptoids.<sup>[4c]</sup>

The possibility that conjugated polymers vitrify from a liquid-crystalline phase resulting in a solid mesophase has also been discussed by Snyder and DeLongchamp.<sup>[4b]</sup> The same authors have also argued that the mesophase of some semiconducting polymers can be considered to be condis crystals,<sup>[4c]</sup> proposing a set of criteria for distinguishing between condis crystals and liquid-crystalline mesophases based, among others, on the birefringence, the entropy of isotropization, and the required undercooling in the order–disorder transition.<sup>[4c]</sup> However, to our knowledge, they have not clearly identified any condis crystal structure in semiconducting polymers so far.

A key contribution in the field was the introduction of the  $g$ -parameter by Salleo and co-workers as a measure of the structural disorder of ordered regions in semiconducting polymers.<sup>[1,17b]</sup> With the assumption that cumulative disorder dominates the width of diffraction peaks in these materials, it has now become a common practice to estimate the  $g$ -parameter from first-order GIWAXS peaks as  $g \approx \frac{1}{2\pi} \sqrt{\Delta q \cdot d_{hkl}}$ , where  $\Delta q$  and  $d_{hkl}$  are the full-width-at-half-maximum (FWHM) and the  $d$ -spacing of the diffraction peak.<sup>[17b]</sup> The analysis of the  $(0k0)$  peaks of PBTTT indicated a dominance of the cumulative lattice disorder and a  $g \approx 8\%$ , thus suggesting paracrystalline order in the solid mesophase in this material.<sup>[1,17b]</sup> Moreover, because paracrystalline domains in nonstretched polymers can be assumed to form through a first-order transition, the conclusion above is contingent upon the observation of a first-order, crystallization-like transition in PBTTT at temperatures in between that of the order–disorder transition and room temperature.<sup>[4c]</sup> However, benzodithiophene polymers do not seem to exhibit such kind of first-order transition at intermediate temperatures (nor has a vitrification been detected).<sup>[3]</sup> Furthermore, typical  $g$ -parameters found in benzodithiophene polymers feature values close to 20% for both the  $(h00)$  and the  $(0k0)$  stack of planes.<sup>[2c]</sup> As mentioned above, these values are well-above those of typical paracrystalline materials, which exhibit  $g$ -parameters ranging from 4% to 12%.<sup>[4b,10b]</sup> In fact,  $g$ -values of  $\approx 20\%$  suggest that benzodithiophene polymers are structurally disordered (even though they are not).<sup>[3]</sup> Thus, there remain many open questions and contradictions on the nature of the mesophase of high-performing benzodithiophene polymers.

The analysis of the mesophase becomes challenging because the mesophase may not be the only aggregate state in the material. While vitrified liquid crystals and paracrystals of stretched polymers tend to extend over most—if not all—the material,<sup>[4c,23]</sup> condis, hexagonal and columnar phases can exhibit a biphasic microstructure where structurally disordered, amorphous-like regions coexist together with the mesophase. If both ordered and disordered regions possess reduced size, as seems to be the case in benzodithiophene-based polymers,<sup>[3]</sup> their independent contributions to experimental signals can be challenging to separate. Indeed, likely influenced by the classical semicrystalline model, it has been widely accepted that disordered regions and ordered regions (mesophase) exist in most

of semiconducting polymers,<sup>[1,24]</sup> including benzodithiophene polymers. However, although microscopy images are compatible with this assumption,<sup>[3]</sup> the disordered (amorphous-like) regions in benzodithiophene-based polymers have not been strictly identified yet as i) the glass transition process of glassy regions has never been observed,<sup>[3,25]</sup> ii) their diffraction pattern does not exhibit an amorphous halo from backbones, and iii) unlike ordered regions, disordered material is hardly visible by transmission electron microscopy (TEM). Hence, also at the length scale of the solid-state microstructure/morphology, there exist open questions that need to be answered regarding the structure of benzodithiophene polymers for OPV.

Importantly, moreover, both aggregate states in benzodithiophene polymers, i.e., the solid mesophase and the disordered phase, are far from thermodynamic equilibrium. Hence, they are expected to spontaneously evolve toward more equilibrated thermodynamic states. Consequently, the microstructure of benzodithiophene-based polymers is expected to be highly sensitive to the temperature (similarly to that of semicrystalline polymers). Resolving their thermotropic phase behavior is thus of paramount importance not only to gain a full structural understanding of these materials but also to be able to design of optimized thermal postdeposition treatments in organic electronic devices.

In this paper, we investigate the structure of spun cast thin films of benzodithiophene-based polymers at different relevant length scales, from the nano- to the mesoscale. On a short length scale, the solid aggregate states are investigated, with particular emphasis on understanding the solid mesophase. Furthermore, we provide a first direct proof of the existence of structurally disordered, glassy regions in these materials. At a larger scale, we investigate how these aggregate states are combined, i.e., their solid-state microstructure/morphology. Finally, the thermotropic phase behavior of benzodithiophene-based polymers is resolved and the effect of thermal annealing of the structure of these materials explained. The above is explored through the behavior of three different semiconducting polymers that have benzodithiophene building blocks in their backbones, the chemical structures of which are shown in Figure 1a–c. The benzodithiophene unit is combined with a fluorinated benzotriazole in PBnDT-FTAZ,<sup>[26]</sup> with a dithienobenzothiazole in PBDB-T-Cl and with a benzodithiophenedione in D18. In addition to those building blocks, the backbones of these three materials also comprise thiophene units. We should note, though, that the benzodithiophene building block is slightly different in the three polymers. Consequently, the focus of this paper is primarily on identifying common structural aspects among the materials rather than on explaining their differences based on their chemical structures.

## 2. Results

### 2.1. Characterization of the Solid-State Microstructure/Morphology

In good agreement with the literature, spun cast PBnDT-FTAZ, PBDB-T-Cl, and D18 thin films exhibit a biphasic nanomorphology, i.e., a solid-state microstructure/morphology that includes two different aggregate states.<sup>[27]</sup> Atomic force microscopy (AFM) phase contrast images of PBnDT-FTAZ, PBDB-T-Cl, and D18

thin films, shown in Figures 2a–c and S2 (Supporting Information), show two regions of disparate mechanical behavior, which, according to the results that will be discussed below, we attribute to differential molecular packing characteristics.<sup>[27b]</sup> Specifically, the mechanically more rigid regions are associated with domains in which molecules are more densely packed, i.e., with the solid-mesophase, while the softer regions include more disordered molecules. Similarly to polymers such as PBDB-T and PM6,<sup>[27b,c]</sup> structurally ordered regions are elongated in PBDB-T-Cl and D18 films. In contrast, these regions are round in PBnDT-FTAZ films, similar to those observed in PTB7.<sup>[27d]</sup> The average characteristic structural length scale of the biphasic morphology is  $\approx 45$  nm for PBnDT-FTAZ, 51 nm for PBDB-T-Cl, and 64 nm for D18, as determined by power spectral density (PSD) analysis (Figure 2d) extracted from the AFM  $5 \mu\text{m} \times 5 \mu\text{m}$  height images shown in Figure S2 of the Supporting Information. This value is likely related to the average distance between mesophase regions.

The presence of structurally ordered regions in these materials was demonstrated from the combination of high-resolution transmission electron microscopy (HRTEM) and GIWAXS. The HRTEM image of a D18 film included in Figure 2e displays regions with periodic molecular packing. Having a pitch of  $\approx 0.3$  nm, we hypothesize that this periodicity corresponds to the (010) plane stack (i.e.,  $\pi$ -stacked chain segments), whose  $d$ -spacing amounts to 0.37 nm ( $q_{(010)} = 16.9 \text{ nm}^{-1}$ ), according to GIWAXS results. As mentioned earlier, GIWAXS patterns of the as-cast PBnDT-FTAZ, PBDB-T-Cl, and D18 thin films (shown in Figure 1d–f) are characterized by broad (100) and (010) peaks that are attributed to the periodic alternation of aromatic backbones and aliphatic side chains, and the lateral packing of backbones, respectively. Additionally, PBDB-T-Cl and D18 exhibit the (00 $l$ ) series of peaks, which is associated with spatial correlations along the aromatic backbones. X-ray coherence length ( $L_c$ ) values were calculated as  $L_c = \frac{2\pi K}{\Delta q}$  from the (100), the (010) and the (001) reflections, where  $\Delta q$  is the FWHM of the peaks and  $K$  is a shape factor, which is here considered to be equal to 1. The  $L_c$  for the D18 (010) peak here is 2.6 nm, which is around 7 molecular layers in the direction of the  $\pi$ - $\pi$  stacking. This value is in good agreement with the HRTEM image shown in Figure 2e and indicates that the structural order in D18 exceeds that typically referred as short-range-order. In addition to the above-mentioned peaks, D18 and PBDB-T-Cl polymers feature a (00 $l$ ) series of peaks, which is attributed to correlations along the aromatic backbone chains. The lack of reflections associated with the ordering of side chains indicates that the side chains are not incorporated in crystalline domains.<sup>[28]</sup>

In order to gain information on the orientation of chains within the fibrillar domains observed in D18 and PBDB-T-Cl samples, a new set of experiments was performed. Here, spun cast D18 films were subject to mechanical rubbing with the aid of a home-made apparatus (Figure S3, Supporting Information). For the following discussion, the rubbing direction is established as parallel to the  $x$ -direction, according to the schematic included in Figure 3a. We must note that, in order to preserve the fibrillar nanomorphology, the rubbing was performed at 200 °C, i.e., at a temperature well-below the melting temperature of the mesophase. AFM images of rubbed films, shown in Figure 3b,c, demonstrate the preferential alignment of the long axis of fibrils along the rubbing direction, i.e., the  $x$ -direction (we note that

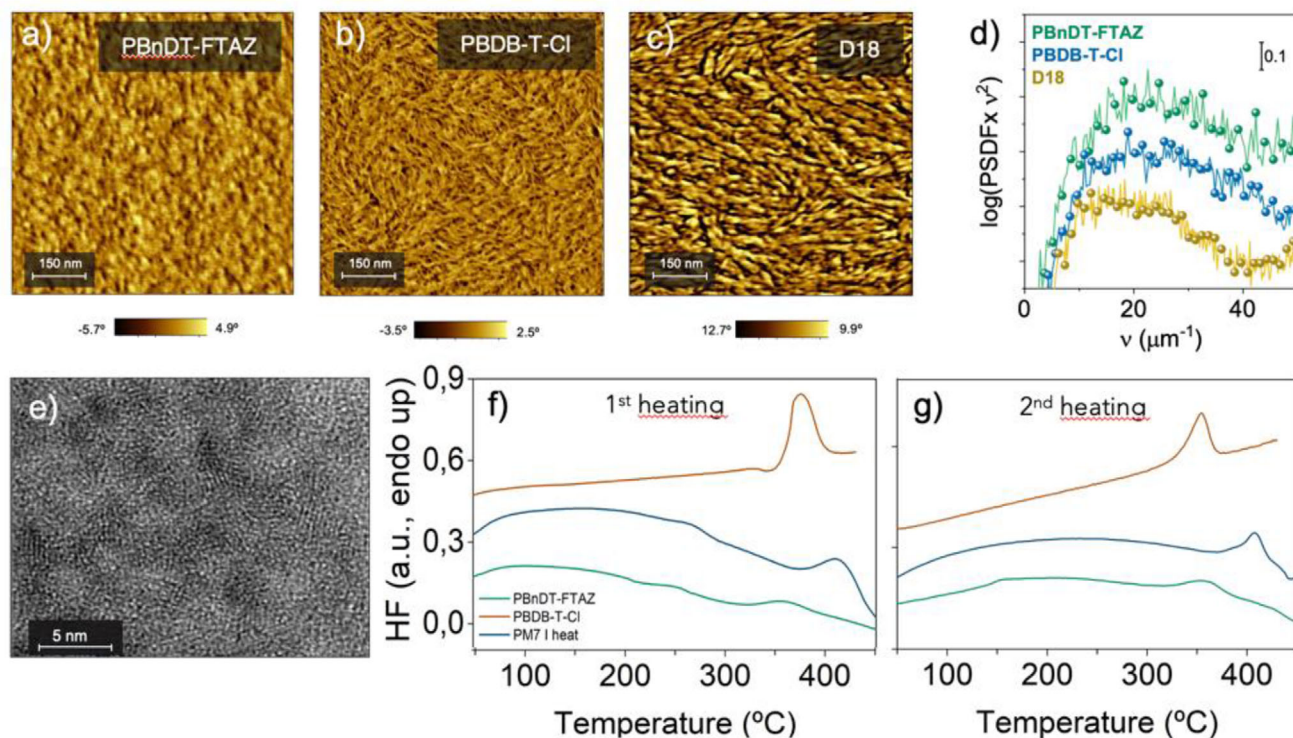


**Figure 2.** AFM phase-contrast images for a) PBnDT-FTAZ, b) PBDB-T-Cl, and c) D18 spun cast thin films. d) Power spectral density profiles extracted from the AFM 5 μm × 5 μm height images shown in Figure S2 of the Supporting Information. e) HRTEM image of a D18 film. f, g) Representative fast scanning calorimetry (FSC) 1st (f) and 2nd (g) heating traces (raw data, at 4000 °C s<sup>-1</sup>) for PBnDT-FTAZ, PBDB-T-Cl, and PBDB-T-Cl.

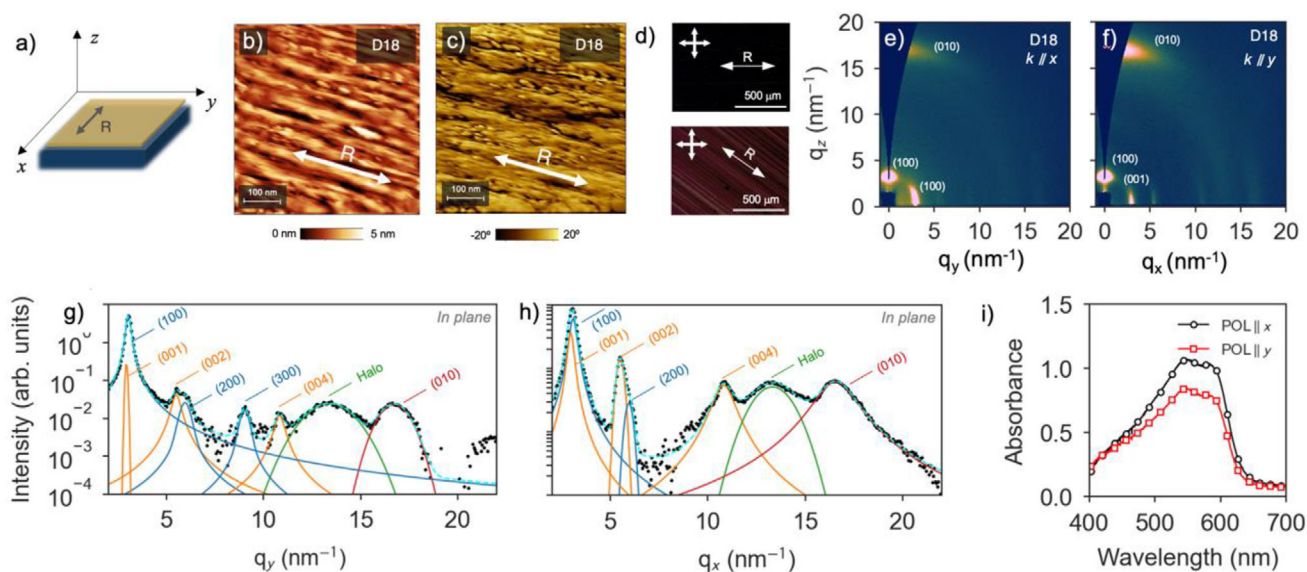


**Figure 3.** a) Schematic showing the spatial directions considered in the experiments. Rubbing direction is parallel to the x-axis. b) AFM topography and c) phase contrast images of rubbed D18 films, where the rubbing direction is indicated. d) Crossed-polarized optical microscopy images of a rubbed D18. The arrows mark the rubbing direction. Room temperature 2D-GIWAXS patterns for D18 films acquired when the electric field of incident X-rays traveled e) along the y-axis and f) along the x-axis (hence, parallel and perpendicular to the rubbing direction). g, h) Corresponding equatorial (in-plane) profiles. i) Polarized absorbance spectra of a rubbed D18 film with the incident polarization direction set parallel (black circles) and perpendicular (red squares) to the rubbing direction.

analogous data for PBDB-T-Cl are included in Figure S4, Supporting Information). Polarized optical microscopy (POM) images included in Figure 3d demonstrated that rubbed films were opaque when rubbing direction lied parallel to any of the polarization axis (0°, 90°, Figure 3d, top), while they were birefringent when the rubbing direction was parallel to the bisector (45°) of the cross-polarization axis (Figure 3d, bottom). Under the initial assumption that the transition dipole moment is parallel to the axis of the conjugated backbone, this data suggests that polymer backbones lie either parallel or perpendicular to the long axis of the fibrils.

Rubbed films were then investigated by GIWAXS with the incident X-ray beam propagation vector direction,  $k$ , (hence the electric field of incident X-rays) traveling parallel (Figure 3e) and perpendicular (Figure 3f) to the rubbing direction, hence parallel to the  $x$ -axis and the  $y$ -axis, respectively. Because the mesophase in D18 exhibits a (00 $l$ ) peak series that are correlated with electron density fluctuations along the aromatic backbones, the location of these peaks in the GIWAXS pattern informs about the direction of backbones. However, in the case of D18, the (001) peak and the (100) peak, appear at very similar  $q$ -values, and their intensities frequently overlap, preventing further information about chain orientation. However, as shown in Figure 3g,h, the (001) peak and the (100) peak are moderately decoupled in rubbed films (see also Figure S5, Supporting Information). Specifically, the (00 $l$ ) peak series appear preferentially along the  $x$ -direction (i.e., the rubbing direction). From AFM we knew that the long axis of the nanofibrils orients parallel to the  $x$ -direction (i.e., the rubbing direction), therefore, we concluded that polymer backbones are oriented preferentially along the long axis of the nanofibrils. This result was further confirmed by linearly polarized UV–vis absorption spectroscopy, with the polarization set parallel and perpendicular to the rubbing direction, i.e., parallel to the  $x$ -axis (POL|| $x$ ) and the  $y$ -axis (POL|| $y$ ), respectively. The greater absorption when the incident light is polarized along the  $x$ -axis confirms that polymer backbones are preferentially aligned along the  $x$ -axis, i.e., along the long axis of fibrils

The presence of structurally disordered regions is, as already mentioned, more challenging to demonstrate, although they can be indirectly detected. Figure 2f,g shows fast scanning calorimetry (FSC) first and second heating scans (performed at 4000 °C s<sup>-1</sup>). For PBDB-T-Cl and D18, the area of the endothermic peaks showing up in the first heating scans is greater than that recorded during the second heating scan. In regular semicrystalline polymers, this would be interpreted as a larger fraction of crystalline material melting in the first compared to the second heating ramps. As it will be discussed later in the paper, the endothermic peak detected here can also be associated with the melting of structurally ordered regions, i.e., with the melting of the mesophase. Consequently, this result can be interpreted by assuming that a fraction of the ordered material that melts in the first heating scan does not melt in the second heating scan. This is most likely because, during the second heating scan, the alluded fraction of material was already disordered at temperatures below the phase transition and hence does not contribute to the melting peak. Thus, this argument is contingent upon the presence of structurally disordered, amorphous-like regions in the material. Furthermore, in Section 2.4 of this paper, we will demonstrate that PBnDT-FTAZ undergoes physical ageing

(i.e., a spontaneous reduction of the enthalpy level of a glass because of structural rearrangements), which demonstrates the presence of glassy (disordered) regions. Moreover, from those experiments we characterize the  $T_g$  of amorphous regions to be between 160 and 200 °C. Interestingly, the second heating trace for PBnDT-FTAZ in Figure 2g exhibits a step-like increase of the heat-flow-rate signal at  $\approx 160$  °C, which can thus be associated with the  $T_g$  of disordered regions in the material.

A further conclusion that can be extracted from the FSC data shown in Figure 2f,g is that despite exhibiting similar nanomorphologies, the benzodithiazole-based polymers investigated here appear to display markedly different fractions of structurally ordered regions. Both first and second heating traces demonstrate comparatively distinct peak areas for the melting peaks of the three polymers, which correlate directly with the amount of ordered material undergoing the phase transition. Given that the masses and latent heats of the samples are unknown, it is not possible to make a quantitative comparison of the fraction of mesophase in these samples using FSC. However, an examination of the peak areas in comparison with the amplitude of their baselines suggests that the melting peaks in D18 are the most intense, followed by PBDB-T-Cl and, lastly, by PBnDT-FTAZ. Consequently, we can argue that D18 films are the ones having with the largest fraction of mesophase and PBnDT-FTAZ exhibit the smallest fraction. In good agreement with this interpretation, AFM images in Figure 2 showed that structurally ordered regions are more densely packed in PBDB-T-Cl and D18 than in PBnDT-FTAZ.

## 2.2. Characterization and Discussion on the Solid Mesophase

The in situ temperature-resolved GIWAXS experiment shown in Figure 4a shows that the (100) and the (010) peaks of the solid mesophase of PBnDT-FTAZ begin to disappear approximately at  $\approx 320$  °C during heating. In other words, molecular correlations along both the lamellar and the  $\pi$ - $\pi$  stacking directions cease to exist approximately at the same temperatures. In fact, a closer look at the in situ GIWAXS data acquired during melting (Figure 4c) reveals that both the intensity of the (100) peak and the calculated  $L_c$  begin to decrease at slightly lower temperatures than those of the (010) peak. This suggests a markedly distinct thermal behavior compared to common layered mesophases, like sanidics and smectics, whose lamellar order disappears at much higher temperatures than the internal order within the layers.<sup>[11b-d,29]</sup> Moreover, we observed that concomitantly with the disappearance of the GIWAXS peaks, the material begins to flow (Figure 4b; Figure S6, Supporting Information). Altogether, these results indicate the order–disorder transition and the solid–liquid transition in benzodithiophene-based polymers occurs almost simultaneously in benzodithiophene polymers. Once again, this is a markedly different behavior compared to that of typical layer-forming liquid crystals, e.g., smectic or sanidic, for whom the order–disorder transition and the solid–liquid transition are independent events.<sup>[22]</sup> In good agreement with the conclusion above, just a single thermal process is observed in FSC heating traces of PBnDT-FTAZ, D18, and PBDB-T-Cl shown in Figure 2i. More specifically, a prominent endothermic peak shows up in the same temperature where the order–disorder and the solid–liquid

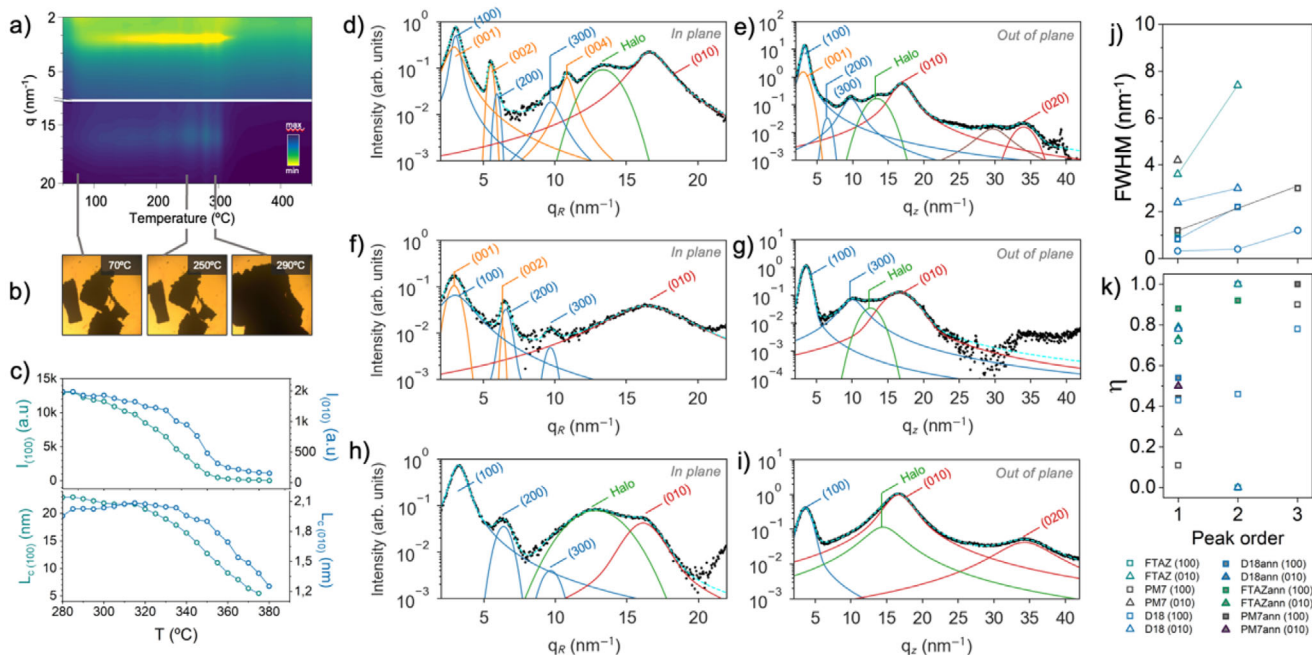


**Figure 4.** a) Contour plot of the azimuthal integrations of the 2D GIWAXS patterns acquired during heating PBnDT-FTAZ from room temperature up to 450 °C at 10 °C min<sup>-1</sup>. b) Optical microcopy images of fine PBnDT-FTAZ powder acquired at selected temperatures during heating from room temperature up to 350 °C at 10 °C min<sup>-1</sup>. Before image acquisition, samples were slightly smashed to check whether they lose their shape at that temperature. c) GIWAXS intensity (azimuthal integrations of 2D patterns) and calculated  $L_c$  during the melting of the layered mesophase in PBnDT-FTAZ. d) In-plane and e) out-of-plane GIWAXS profiles for D18. f) In-plane and g) out-of-plane GIWAXS profiles for PBDB-T-Cl. h) In-plane and i) out-of-plane GIWAXS profiles for PBnDT-FTAZ. Peaks are fitted to pseudo-Voigt functions. j) FWHM and k) pseudo-Voigt mixing parameter,  $\eta$ , as a function of peak order. Empty and filled symbols correspond to as-cast and thermally annealed (at 200 °C) samples.

transition are detected. Thus, this endothermic peak can be associated with the melting of the solid mesophase. We should note that thermal transitions can undergo a shift to higher temperatures in FSC due to the thermal lag resulting from the rapid heating rates employed.

However, despite exhibiting a single phase transition, the GIWAXS results of benzodithiophene-based polymers suggest a layered structure like those in smectic and sanidic liquid crystals. Figure 1d–f shows the 2D-GIWAXS patterns and Figure 4d–i shows the corresponding in-plane and out-of-plane profiles. Condis crystals, columnar phases, hexagonal phases, and paracrystals tend to exhibit long-range order in the two dimensions perpendicular to the chain axes, along which polymer chains are stacked.<sup>[9,13b]</sup> This condition is fulfilled in the case of the semiconducting polymers investigated in this work as crystallographic registers along  $[h00]$  and  $[0k0]$  directions are detected. However, these peaks lack the radial symmetry that should be expected in columnar mesophases. For example, the (010) appears almost exclusively along the  $z$ -axis when the incident beam travels parallel to the chain direction, i.e., along the  $x$ -axis (see Figure 3e). A certain radial symmetry would have resulted in the manifestation of (010) reflections at positions other than just the meridian of the  $z$ - $y$  plane.<sup>[13a]</sup> For example, in columns arranged in a hexagonal fashion,<sup>[8]</sup> the (010) reflections would show up in regions of the  $z$ - $y$  plane that are separated 60° (along the azimuthal angle). Or, alternatively, if columns (or group of columns) exhibit a certain  $d$ -spacings but random-like orientation in the  $z$ - $y$  plane, the 2D GIWAXS would show an isotropic

distribution of the (010) peak intensity. We note, moreover, that this argument is equally valid for the ( $h00$ ) reflections. The layered periodicity of the mesophase occurs along the direction perpendicular to the ( $h00$ ) planes, as it can be deduced from the observation of periodically spaced higher-order ( $h00$ ) peaks. Hence, backbones and side chains phase separate into a structure with lamellar periodicity (with an  $\approx 2$  nm pitch), where the two layers exhibit different density, molecular mobility and thermal behavior, as will be shown in a subsequent section of the paper. Such structure is thus closer to self-assembled systems, such as liquid crystals, amphiphilic molecules or block copolymers, than to typical condis crystals, paracrystals, and columnar phases in general, which typically exhibit more-continuous, nonseparated structures.

A further characteristic that alienates the mesophase of benzodithiophene polymers from typical hexagonal phases is the presence of well-defined spatial correlations along the aromatic backbones, reflected in (00 $l$ ) peaks (at least in D18 and PBDB-T-Cl). As already mentioned, a common feature of condis crystals, hexagonal phases and (micro)paracrystals is the absence of positional long-range order along the chain direction due to intrinsic conformational disorder. Conversely,  $L_c$  along the chain direction, as measured from the (001) peak of rubbed D18 film (Figure 3h), amounts to 19 nm, demonstrating long-range-positional order in this direction. The  $L_c$  calculated from the (001) of nonannealed and nonoriented D18 film was  $\approx 5$  nm.

In order to gain more information about the mesophase, GIWAXS peak fit analysis was conducted. Here again, peaks were

fitted to pseudo-Voigt functions (Figure 4d-i) and fitting parameters are included in Table 1. The analysis reveals the increase in FWHM of (0k0) and (h00) peaks with increasing diffraction order (Table 1 and Figure 4j), suggesting that peak widths, hence the  $L_c$ s, are largely dominated by lattice disorder rather than the finite size of crystallites. In contrast, the weak dependence of the peak width with the diffraction order of the (00l) series suggests that the  $L_c$  of the (001) peak reflects more suitably the crystallite size along chain direction. The  $L_c$  values measured from the (100) peak were 5.2, 5.8, and 7.7 nm for PBnDT-FTAZ, PBDB-T-Cl, and D18, respectively, which correspond roughly to 3–4 molecular layers along the lamellar periodicity. On the other hand, the  $L_c$  values calculated from the (010) peaks were 1.8, 1.5, and 2.6 nm for PBnDT-FTAZ, PBDB-T-Cl, and D18, respectively, which correspond to  $\approx 5$ ,  $\approx 4$ , and  $\approx 7$   $\pi$ -stacked molecular layers. As mentioned above, the  $L_c$  calculated from the (001) of nonannealed and nonoriented D18 film was 5.0 nm.

In agreement with previous results on similar materials,<sup>[2c]</sup> peak-fit analysis reveals remarkable high  $g$ -parameter values for the (100) and the (010) peaks (Table 1). The  $g$ -parameters measured for the (100) planes of D18, PBDB-T-Cl, and PBnDT-FTAZ were 19.9%, 23.2%, and 23.4%, respectively, while the  $g$ -parameters for the (010) planes amounted to 15.1%, 18.5%, and 20.2%, respectively. These values are well-beyond the range for structurally ordered materials in the standardized  $g$ -parameter scale (i.e.,  $g < 12\%$ ) and thus suggest a predominantly disordered molecular packing in both the (h00) and (0k0) series of planes (Table 1).<sup>[4b]</sup> However, this interpretation clearly contradicts the data set shown above (e.g., FSC, TEM, AFM, etc.), which clearly revealed the presence structural order in these materials (Figure 2). We argue that this apparent discrepancy may have different origins: On the one hand, it can result from the coexistence of various aggregate states with different degrees of structural order,<sup>[10b,30]</sup> the contribution of which to the  $g$ -parameter cannot be well-resolved in common GIWAXS experiments. Thus, the  $g$ -parameter as extracted from 1st order peak may overestimate the degree of disorder of the mesophase simply because it includes the contribution of amorphous regions. On the other hand, the peak width in some of these materials may not be dominated by cumulative disorder, which is an implicit condition in the calculation of the  $g$ -parameter through 1st order peaks.<sup>[17b]</sup> The non-Lorentzian shape of the (100) and (010) peaks in, e.g., in PBDB-T-Cl, as reflected in the low values of the pseudo-Voigt mixing parameters,  $\eta$ , indicate a significant—if not dominant—contribution of statistically random lattice-parameter fluctuations to the overall disorder (Table 1 and Figure 4k).<sup>[2c,31]</sup> Interestingly, the contribution of cumulative disorder to the overall lattice disorder increases in thermally annealed samples, suggesting that the homogeneity of lattice parameters in the mesophase improves upon thermal annealing (Figure 4k; Table S1, Supporting Information).

All in all, the solid mesophase in semiconducting polymers for OPV at regular device operation temperatures (e.g., below 80 °C) seems to be a layered structure in which solid-like (e.g., rigid) layers of  $\pi$ -stacked aromatic backbones and layers of highly mobile (liquid-like) aliphatic side chains are alternated. According to GIWAXS, such lamellar periodicity extends over at least 3–4 molecular layers in the as-cast films (Figure 5). Within aromatic layers, backbone chains are laterally packed in a highly

**Table 1.** GIWAXS peak fitting analysis for the as-cast PBDB-T-Cl, PBnDT-FTAZ, and D18 films.

|            | (100)      |         |                          | (200)  |                          |                       | (300)                    |                    |            | (010)   |                          |        | (020)             |                    |                          | (001)  |                    |         | (002)                    |                    |                          | (004)              |                          |                      |   |
|------------|------------|---------|--------------------------|--------|--------------------------|-----------------------|--------------------------|--------------------|------------|---------|--------------------------|--------|-------------------|--------------------|--------------------------|--------|--------------------|---------|--------------------------|--------------------|--------------------------|--------------------|--------------------------|----------------------|---|
|            | $L_c$ [nm] | $g$ [%] | FWHM [nm <sup>-1</sup> ] | $\eta$ | FWHM [nm <sup>-1</sup> ] | $\eta$                | FWHM [nm <sup>-1</sup> ] | $\eta$             | $L_c$ [nm] | $g$ [%] | FWHM [nm <sup>-1</sup> ] | $\eta$ | $L_c$ [nm]        | $g$ [%]            | FWHM [nm <sup>-1</sup> ] | $\eta$ | $L_c$ [nm]         | $g$ [%] | FWHM [nm <sup>-1</sup> ] | $\eta$             | FWHM [nm <sup>-1</sup> ] | $\eta$             | FWHM [nm <sup>-1</sup> ] | $\eta$               |   |
| PBDB-T-Cl  | 5.2        | 23.4    | 1.2                      | 0.11   | —                        | —                     | 3.0 <sup>a)</sup>        | 1.00 <sup>a)</sup> | 1.5        | 20.2    | 4.2                      | 0.27   | —                 | —                  | —                        | —      | —                  | —       | —                        | —                  | —                        | —                  | —                        | —                    | — |
| PBnDT-FTAZ | 5.8        | 23.2    | 1.1                      | 0.72   | 1.2 <sup>a)</sup>        | 0.00 <sup>a)</sup>    | —                        | —                  | 1.8        | 18.5    | 3.6                      | 0.79   | 7.4 <sup>a)</sup> | 1.00 <sup>a)</sup> | —                        | —      | —                  | —       | —                        | —                  | —                        | —                  | —                        | —                    | — |
| D18        | 7.7        | 19.9    | 0.82                     | 0.43   | 1.0 <sup>a)</sup>        | 0.46 <sup>a),b)</sup> | 2.2                      | 0.78               | 2.6        | 15.1    | 2.4                      | 0.78   | 3.0 <sup>a)</sup> | 0.00 <sup>a)</sup> | 5                        | 0.84   | 19.3 <sup>a)</sup> | 0.84    | 0.42 <sup>a)</sup>       | 0.94 <sup>a)</sup> | 0.84                     | 0.42 <sup>a)</sup> | 0.84                     | 1.0 <sup>a),c)</sup> |   |

<sup>a)</sup>The peak intensity is too low for a reliable fit analysis; <sup>b)</sup> From the analysis of oriented samples.

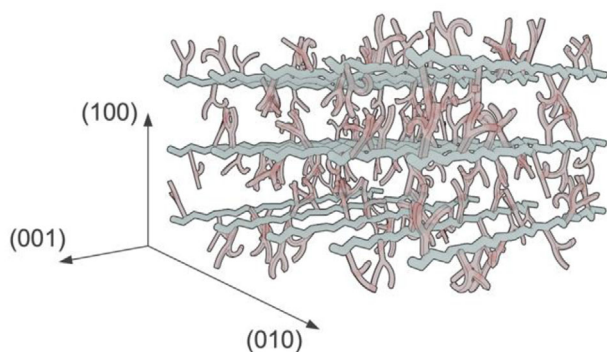


**Figure 5.** Schematic illustration of the mesophase in benzodithiophene-based polymers for OPV. Aromatic backbones appear in gray while aliphatic disordered side chains are shown in red (for the sake of clarity of the schematic, a fraction of side chains are omitted, and intermolecular distances are not drawn in real scale).

imperfect parallel fashion over at least 7  $\pi$ -stacked chain segments. Moreover, due to the rigidity of the backbones, aromatic layers exhibit some long-range order along the chain direction. Consequently, aromatic layers might be seen as a sort of 2D columnar (or condis or paracrystalline) mesophase. Side-chain layers, however, show liquid-like disorder. A particular feature that differentiates this mesophase from other layered mesophases reported previously in the literature, e.g., sanidics and smectics, is that structural order within aromatic layer seem to disappear at similar (or even slightly higher) temperatures than lamellar periodicity, which is why the order–disorder transition and the solid–liquid transition in benzodithiophene-based polymers occurs approximately at the same temperature. In other words, upon heating, the stack of platelets is disrupted almost simultaneously to the collapse of the platelets. It is important to note that this polymer mesophase seems to be also present in donor:acceptor blends used in high-performing OSCs, as the GIWAXS patterns of many donod:acceptor BHJs are similar to those of neat polymers (Figure S7, Supporting Information).

### 2.3. Characterization of the Thermotropic Behavior

To complement the analysis of the solid-state microstructure of PBDB-T-Cl, D18, and PBnDT-FTAZ spun cast films, an investigation was conducted into their thermotropic behavior. In situ temperature-resolved GIWAXS (see, e.g., Figure 4a; Figure S8, Supporting Information) did not yield any insights into the phase behavior of these materials. This is to be expected, given that GIWAXS is largely sensitive to structures with long-range positional order, while aggregate states with greater disorder, such as amorphous phases, are challenging to characterize using GIWAXS. Similarly, temperature-resolved POM analysis did not yield further insights, as these materials are not birefringent at any temperature (see Figure S9, Supporting Information). In contrast, FSC is sensitive to changes in the specific heat capacity ( $c_p$ ) and enthalpy ( $\Delta H$ ) of samples. Given that any structural change in both structurally ordered and disordered material's regions results in  $c_p$  and  $\Delta H$  changes, FSC is an excellent method for investigating the thermotropic phase behavior of semiconducting polymers. Furthermore, FSC has two additional benefits: i) the

rapid heating and cooling rates (up to 10 000 °C s<sup>-1</sup>) minimize thermal degradation of samples at elevated temperatures, and ii) spin-cast thin films, as those commonly used in devices (such as solar cells), can be investigated. Here, we will focus our discussion on PBDB-T-Cl and PBnDT-FTAZ, because D18 and PBDB-T-Cl have very similar thermotropic behavior, as will be shown below.

Because each aggregate state (e.g., a solid mesophase, a disordered glass, a crystal, a supercooled liquid, a liquid-crystalline mesophase, etc.) exhibits a different response to the temperature, a first set of experiments were designed to ascertain the temperature ranges within which the materials displayed disparate calorimetric responses. These temperature ranges are thus directly correlated with the aggregate states present in the material. Furthermore, the temperatures demarcating the boundary between these temperature regions will correspond to the phase transition temperatures. To this end, the FSC experimental protocol depicted in Figure 6a was performed. Initially, the materials were subjected to a temperature exceeding the order–disorder transition, thereby eliminating any thermal history (e.g., 420 °C). Subsequently, the samples were rapidly cooled (at 4000 °C s<sup>-1</sup>) to a specific isothermal temperature ( $T_a$ ), which ranged from –80 to 280 °C, and maintained at those conditions for 60 min. During this isothermal period, a certain aggregate state of the material will undergo evolution in accordance with the dictates of its thermodynamic properties. To illustrate this, if  $T_a$  falls within the temperature range in which a material contains a glassy state, the glass will undergo physical aging. Conversely, if  $T_a$  is within the temperature range in which the material contains a supercooled liquid state, the system will attempt to crystallize via cold crystallization. In both scenarios, the structural evolution of the material at each temperature can be investigated through a subsequent heating scan (denoted as A in Figure 6a). For instance, the physical aging of the glass during the isothermal step results in the emergence of an endothermic overshoot at temperatures proximate to the  $T_g$  in the subsequent heating scan. Likewise, if crystallinity has developed during the isothermal step, the subsequent heating scan will display an endothermic peak, reflecting the melting of the newly formed crystallites. Conversely, if  $T_a$  is a temperature above the melting temperature ( $T_m$ ), the material will not undergo any thermodynamic evolution during the isothermal step, as the liquid is already in thermodynamic equilibrium. Consequently, the subsequent heating scan will not display any new signals.<sup>[29,32]</sup> A-heating traces are then compared to the heating trace of the material that has not undergone an isothermal step (hereafter referred to as curve B).

While the raw calorimetric heating traces A and B for PBDB-T-Cl and PBnDT-FTAZ at each  $T_a$  are shown in Figure S10 of the Supporting Information, here we undertake a comparative analysis between them. The subtraction of heating trace B from heating trace A provides the excess heat flow rate of the annealed sample relative to the nonannealed sample ( $\Delta HF$ ) at each  $T_a$ . Thus, any  $\Delta HF$  signal that is not equal to zero indicates that the material underwent a specific structural evolution during the isothermal step at that  $T_a$ . Figure 6b,c illustrates the  $\Delta HF$  versus temperature curves for PBDB-T-Cl and PBnDT-FTAZ, respectively, with the applied  $T_a$ s indicated as a color scale in Figure 6c. It is evident that the isothermal steps result in the emergence of

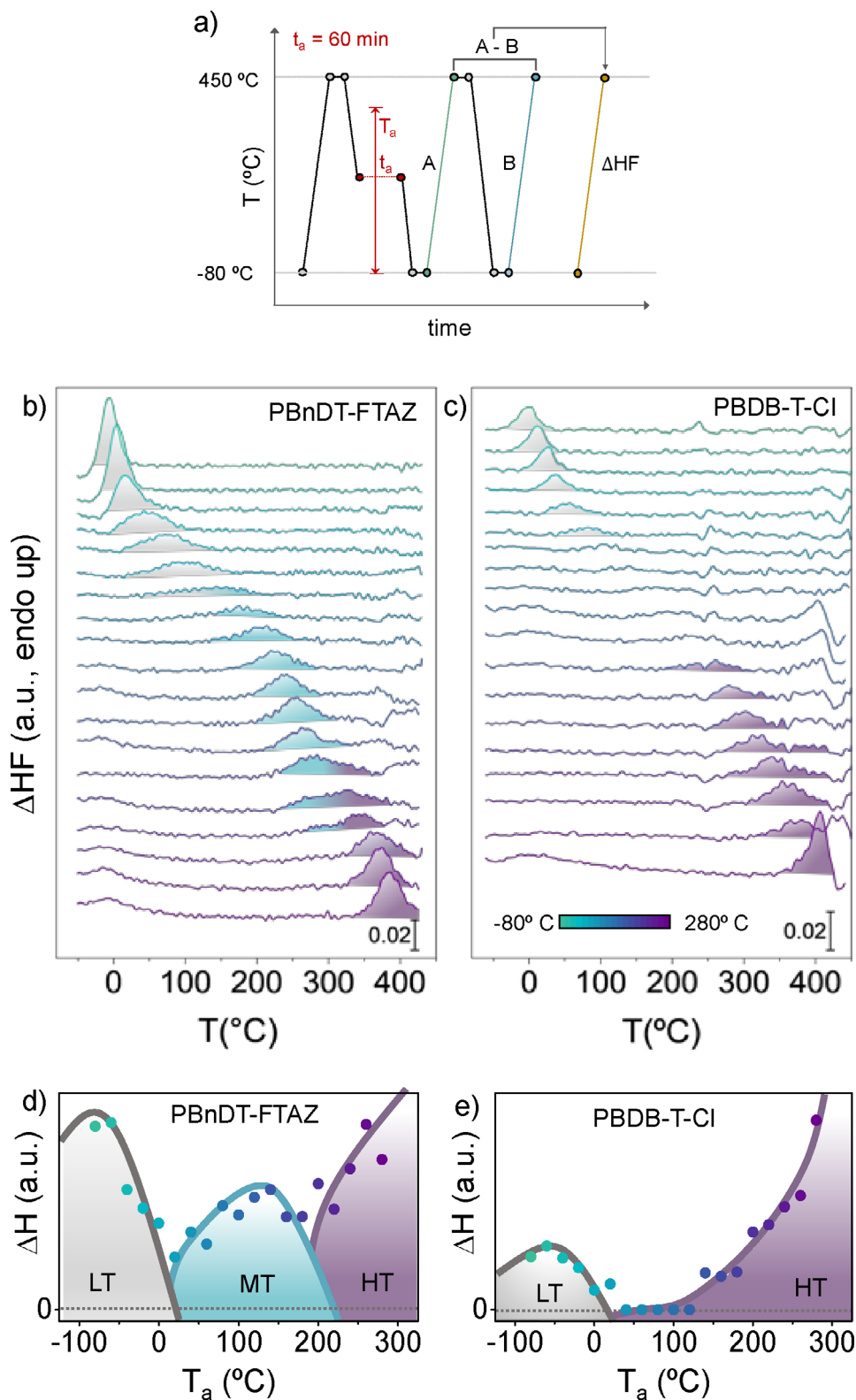


**Figure 6.** a) Thermal profiles applied in FSC experiments. Excess of heat flow rate ( $\Delta HF$ ) for b) PBnDT-FTAZ and c) PBDB-T-CI samples subject to the thermal protocol shown in (a). Isothermal temperatures,  $T_a$ s, ranged from -80 to 280 °C. Enthalpy change,  $\Delta H$ , for d) PBnDT-FTAZ and e) PBDB-T-CI samples calculated from the peaks showing up in (b) and (c) (in arbitrary units) plotted against the annealing temperature,  $T_a$ .

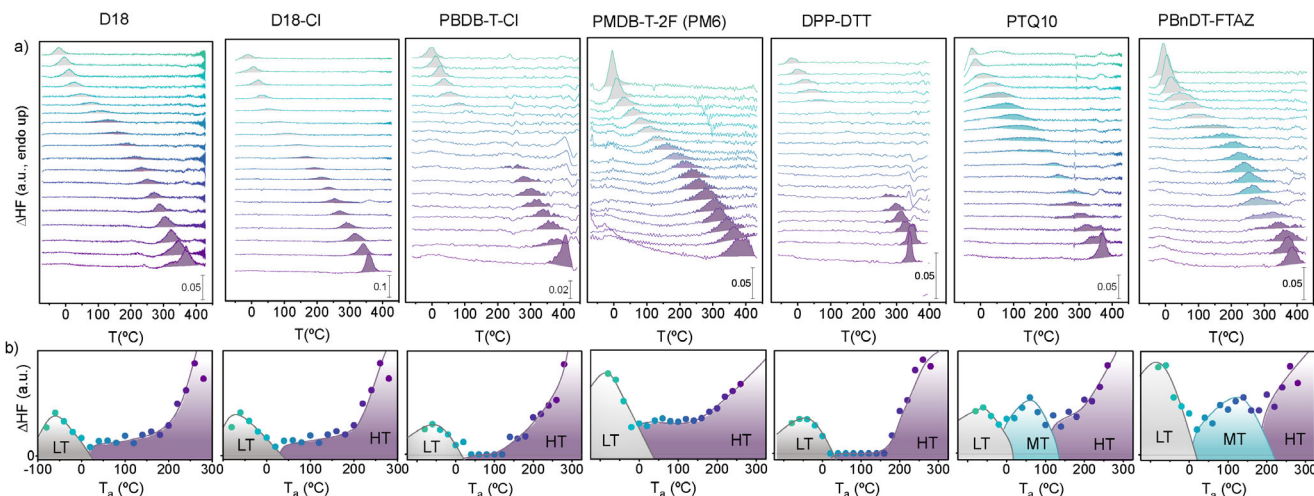


**Figure 7.** a)  $\Delta H F$  for different high-performing donor polymers subject to the thermal protocol shown in Figure 6a. b)  $\Delta H$  calculated from endothermic peaks in  $\Delta H F$  curves plotted versus  $T_a$ s.

endothermic peaks, exhibiting a discernible increase and decrease in intensity depending on the applied  $T_a$ .

Figure 6b illustrates the evolution of three distinct peaks for PBnDT-FTAZ across the temperature range under investigation. In other words, PBnDT-FTAZ has three distinct temperature regions in which it exhibits a different calorimetric response, indicating the presence of at least three different solid aggregate states in the temperature range analyzed. The existence of three relevant temperature regions can be also deduced from the dependence of the endothermic peak with temperature, which is shown in Figure S11 of the Supporting Information).

These temperature regions are designated as the low-temperature (LT) region, the medium-temperature (MD) region, and the high-temperature (HT) region, respectively. An intense peak (shadowed in gray) that disappears at  $\approx 20$  °C is associated with the LT region. The medium-temperature (MT) region is characterized by a peak shadowed in blue, which exists in the temperature range between 20 °C and  $\approx 200$  °C. Lastly, the HT region, which is characterized by the peak shadowed in purple, shows up at  $T_a$ s higher than 200 °C. The two transition regions between these phases at  $\approx 20$  and 200 °C can be readily perceived since these temperatures display a double peak feature.

Figure 6d provides a more detailed illustration of the temperature ranges of these solid aggregate states and the phase transition temperatures. It plots the enthalpy change ( $\Delta H$ ) associated with the structural evolution of PBnDT-FTAZ during the isothermal steps (in arbitrary units) against the  $T_a$ s applied. Therefore, the  $T_a$  at which the  $\Delta H$  is equal to zero corresponds to the upper limit of the phase transition temperature. It must be noted that transitions between aggregate states can be broad, resulting in instances where the calorimetric signature of two or more aggregate states can be detected. For instance, at  $T_a = 180$  °C, both the endothermic peaks associated with the MT and LT states are observed.

Interestingly, when this methodology is applied to PBDB-T-Cl, only two distinct temperature regions are identified: an LT region and an HT region (Figure 6c,e). The LT region is observed at temperatures below 40 °C. The application of  $T_a$ s between 60 and

100 °C does not induce significant structural changes in the material. At temperatures exceeding 100 °C, an endothermic peak associated with the HT state emerges, exhibiting a growing enthalpy with increasing  $T_a$  (up to  $T_a = 280$  °C). Thus, it appears that the MT state is absent in PBDB-T-Cl. We must note that the presence of a triad and a dyad of relevant temperature regions in PBnDT-FTAZ and PBDB-T-Cl, respectively, was confirmed in a further set of FSC experiments that are included in Figure S12 of the Supporting Information, where a sequence of two isothermal steps (in descending and ascending order) was applied.

It is noteworthy that all the exemplary donor polymers for OPV that have been subjected to the FSC experimental protocol outlined in Figure 6a demonstrate a thermotropic phase behavior that is analogous to either that of PBDB-T-Cl or that of PBnDT-FTAZ, see Figure 7a. Their corresponding HF signals recorded for heating scans A and B are shown in Figure S13 of the Supporting Information. Panels in Figure 7b depict the calculated  $\Delta H$  values derived from the endothermic peaks of the  $\Delta H F$  curves plotted against the applied  $T_a$ s. Tellingly, two distinct solid aggregate states, namely, the LT state and the HT state, have been observed in the case of D18, D18-Cl, PBDB-T-2F (PM6), and PBDB-T-Cl (and DPP-DTT). In contrast, polymers such as PBnDT-FTAZ and PTQ10 have been found to exhibit three aggregate states, namely, LT, MT, and HT states.

#### 2.4. Identification of the Aggregate States (and Their Phase Transitions) and Rationalization of the Effects of Thermal Annealing on the Structure

A significant question arises regarding the reason behind the two-phase and three-phase thermotropic behavior observed in D18, D18-Cl, PBDB-T-2F (PM6), and PBDB-T-Cl, and PBnDT-FTAZ, and PTQ10, respectively. To address this question, we investigated the structure of the polymers in the LT, MT, and HT temperature regions. Because all three temperature regions are present in PBnDT-FTAZ, this polymer will be the focus of our

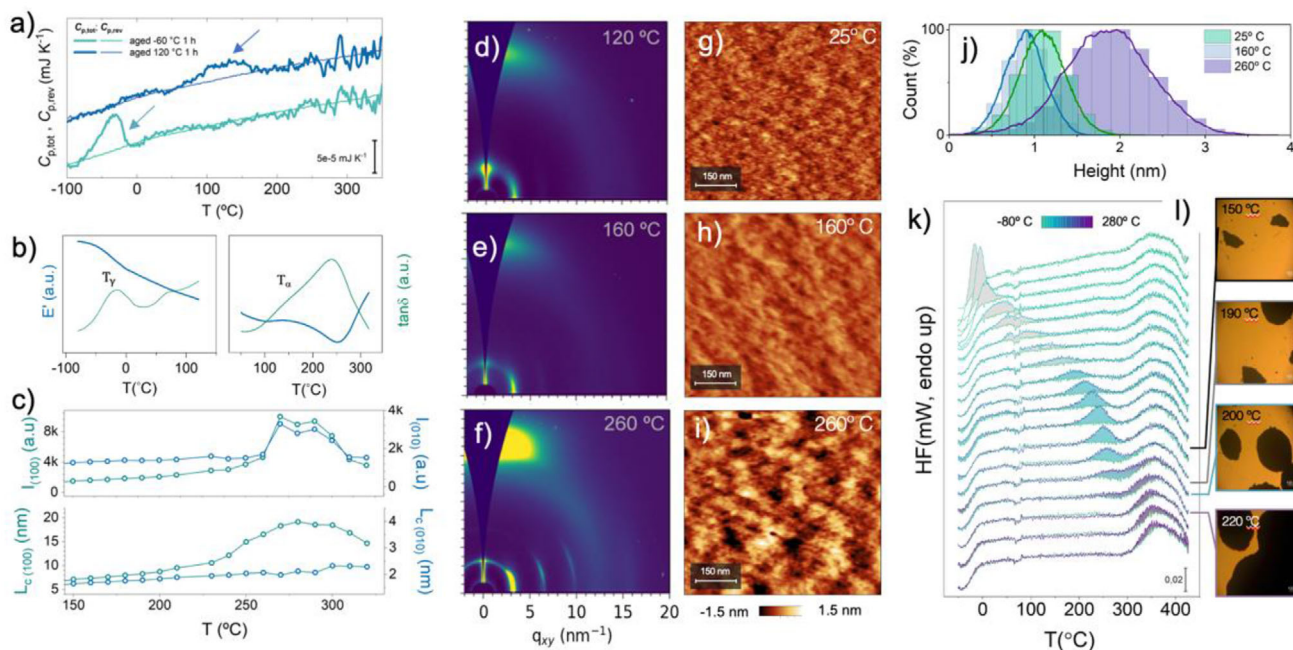


**Figure 8.** a) Frequency-dependent reversing heat capacity,  $C_{p,rev}$  (thin lines) and total heat capacity,  $C_{p,tot}$  (thick lines) signals obtained from step response flash scanning calorimetry experiments during a heating a PBnDT-FTAZ samples that was previously annealed/aged at  $-60$  °C (green lines) and  $120$  °C (blue lines). Endothermic overshoots appearing in the  $C_{p,tot}$  traces are indicated with arrows. b) Storage modulus ( $E'$ ) and  $\tan \delta$  versus temperature from dynamic mechanical analysis (DMA) during heating PBnDT-FTAZ from room temperature up to  $330$  °C at  $10$  °C  $\text{min}^{-1}$ . c) GIWAXS intensity (azimuthal integrations of 2D patterns) and calculated  $L_c$  during heating PBnDT-FTAZ up to  $330$  °C at  $10$  °C  $\text{min}^{-1}$  (the temperature ranges of the MT and the HT regions are illustrated with shaded areas). d–f) GIWAXS 2D patterns and g–i) AFM height images for ex situ annealed PBnDT-FTAZ films. AFM height images. j) Height histograms obtained from the AFM images. k) Heat flow rate (HF) versus temperature curves for heating scans A and B for a PBnDT-FTAZ sample with a large fraction of amorphous regions (thermal protocol applies is shown in Figure 6a). i) Optical microscopy images of PBnDT-FTAZ acquired at selected temperatures during heating from room temperature up to  $350$  °C at  $10$  °C  $\text{min}^{-1}$ .

discussion, while similar data for the counterpart PBDB-T-Cl is included in Figures S14 and S15 of the Supporting Information.

We begin our discussion with the LT region, which corresponds to the thermotropic state of all polymers analyzed below  $\approx 0$  °C. The most relevant calorimetric feature in this phase is an endothermic peak, colored in gray in Figure 6b, appearing in the FSC heating scan after PBnDT-FTAZ is isothermally kept at  $T_a < 0$  °C. We argue that this peak corresponds to the recovery of the enthalpy during the devitrification of glassy regions comprising aliphatic side chains that are confined within the layered mesophase. Thus, in the LT state side-chain layers in the mesophase are in the glassy state. The primary rationale for this interpretation is as follows.

- We associate the endothermic peak with a thermal event occurring to side-chains because the isothermal temperature at which the peak disappears, i.e., the phase-transition temperature, is very similar across all polymers, irrespective of the chain structure of the backbones (see Figure 7). We note that the chemical nature of the side chains is relatively consistent among the polymers under analysis.
- We rule out that the endothermic peak is due to the melting of crystallized side chains, first because no other experimental method used in this work has detected the presence of side-chain crystals; and second, because the peak

does not show up in the frequency-dependent reversing heat capacity  $C_{p,rev}(\omega)$  signal obtained from step response flash scanning calorimetry experiments ( $C_{p,rev}(\omega) = |C_p^*(\omega)| = \sqrt{(C_p'(\omega))^2 + (C_p''(\omega))^2}$  (thin green line in Figure 8a), as it would be the case for a crystal melting process. Similarly to experiments shown in Figure 6b, a prominent endothermic peak is observed in the curve for the total heat capacity ( $C_{p,tot}$ ,  $C_{p,tot} = \frac{\int_0^p \text{HF}(t) dt}{\int_0^p q(t) dt}$ , thick green line in Figure 8a), during the heating scan of a PBnDT-FTAZ that has been isothermally treated at  $-60$  °C (the peak is indicated with an arrow). However, the peak does not appear in the  $C_{p,rev}(\omega)$  curve, indicating that this thermal event is related to an irreversible process, such as the recovery of enthalpy of a physically aged glassy region. Further details of this experiment are included in Figure S16 of the Supporting Information.

- The dynamic mechanical analysis, DMA, data presented in Figure 8b (conducted at  $1$  Hz during heating a glass fiber mesh reinforced PBnDT-FTAZ sample) demonstrates an intense relaxation process, denoted as  $T_\gamma$  on the  $\tan \delta$  curve, occurring at temperatures where the endothermic process disappears. This observation aligns with the hypothesis of devitrification of side-chain domains, a conclusion that is supported by the majority of the existing literature on DMA.<sup>[21b,25,33]</sup>

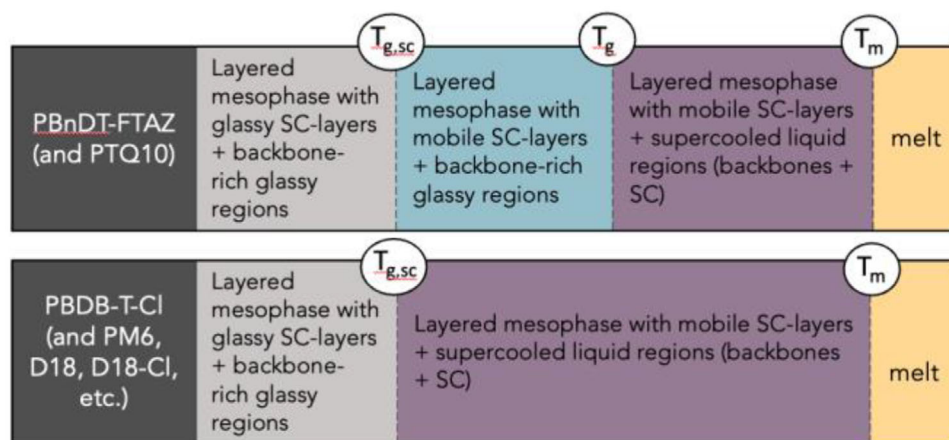


**Figure 9.** Thermotropic phase behavior of benzodithiophene polymers, where the aggregate states present within relevant temperature regions are indicated.  $T_{g,sc}$ ,  $T_g$ , and  $T_m$  correspond to the glass transition temperature of side-chain layers within the mesophase, the glass transition temperature of backbone-rich regions and the melting temperature of the mesophase, respectively.

(d) We argue that solely side chains within the mesophase contribute to the endothermic overshoot observed in FSC because in order to see a structural relaxation (i.e., a glass transition), side-chain domains must be larger than the characteristic length scale associated with the cooperativity of the segmental motions that are relevant for the glass transition. In the vicinity of the  $T_g$ , this length scale is expected to be of 1–3 nm.<sup>[34]</sup> This means that side-chain-rich regions with sizes in the order of magnitude of 1–3 nm exist in these materials, which are unlikely in materials regions other than the mesophase.

Consequently, the LT region is distinguished by the existence of mesophase domains, whose side-chain-rich layers are vitrified, and further backbone-rich glassy regions. Glassy side-chain regions devitrify at its glass transition temperature,  $T_{g,SC}$  in **Figure 9**, which is observed to be  $\approx 0$  °C for all polymers analyzed here. Because  $T_{g,SC}$  is typically lower than the operation temperature of OSCs—indeed lower than room temperature—these side-chain regions are expected to be liquid-like in real devices.

Temperatures immediately above the  $T_{g,SC}$  defines the MT region. Thus, the MT region found in PBnDT-FTAZ combines disordered, glassy domains (composed mainly of backbones) and the layered mesophase where backbones form solid-like layers but aliphatic layers are mobile. Thus, the endothermic peak showing up when samples were isothermally annealed between  $\approx 20$  and  $\approx 220$  °C in **Figure 6** can be attributed to the enthalpy recovery (during the devitrification) of glassy regions comprising PBnDT-FTAZ backbones. Moreover, the minimum  $T_a$  at which this peak is not visible corresponds to the upper limit of the distribution of  $T_g$ s of the material, which is referred to as the  $T_g^{\text{onset}}$ .<sup>[35]</sup> Our data thus reveals that the  $T_g^{\text{onset}}$  of PBnDT-FTAZ vitrified at  $4000$  °C  $s^{-1}$  is between  $220$  and  $240$  °C. However, the intensity of the endothermic peak begins to decrease at  $T_a = 160$  °C, which means that some glassy regions have already devitrified at that temperature, evidencing a broad distribution of  $T_g$ s, thereby a large dynamical heterogeneity of the glassy regions in PBnDT-FTAZ. We would like to note that, to the best of our knowledge, this is the first direct observation of the  $T_g$  of

a benzodithiophene-based semiconducting polymer. Likewise, it constitutes the inaugural direct proof of the existence of structurally disordered, glassy regions in this category of materials. Our hypothesis that the MT state comprises glassy disordered regions that undergo a glass transition is based on the following results.

- As for the LT state, a distinctive endothermic peak is observed in the curve for the  $C_{p,\text{tot}}$  thin blue line in **Figure 8a**, during the heating scan of a PBnDT-FTAZ that has been isothermally treated at  $120$  °C. Here again, the peak does not show up in the  $C_{p,\text{rev}}(\omega)$  curve, indicating that such a peak is associated with the glass transition of a glassy region (further details of this experiment are included in **Figure S16**, Supporting Information).
- In situ GIWAXS results obtained during heating (**Figure 8c**) as well as ex situ GIWAXS (**Figure 8d–f**; **Figure S17**, Supporting Information) and AFM data (**Figure 8g–i**) obtained on samples annealed ex situ at temperatures below  $T_g$ , i.e., at a temperature within the MT state, exhibit minor structural changes compared to nonannealed samples (**Figure 2a**). In this temperature range, disordered regions are in a glassy state, hence the rate of their nonlocal molecular motions is too slow to induce significant structural changes (as shown also in in situ GIWAXS measurements performed during isothermal annealing, **Figure S18**, Supporting Information). Only minor improvement of the layer periodicity of the mesophase is detected through weak increases of the peak intensity and the  $L_c$  of the (100) peak (see **Figure 8c**). This is likely related to the fact that aliphatic layers are mobile and thus are able to promote a certain improvement of the lamellar order. Main structural changes related to ordered regions occur at temperatures higher than the  $T_g$ , like in regular semicrystalline polymers. For example, the appearance of higher order ( $h00$ ) peaks (**Figure 8f**; **Figure S17**, Supporting Information), the increase of both the intensity and the  $L_c$  of (100)  $\gamma$  (010) peaks (**Figure 8c**), the large increase of the film roughness observed in AFM (**Figure 8g–i**) and the for-

mation of new mesophase regions (whose melting peaks can be observed in Figure 6b) occur only at temperatures above  $\approx 200$  °C.

- (c) When a PBnDT-FTAZ sample with a high fraction of disordered domains is analyzed (e.g., a PBnDT-FTAZ with  $M_w = 28 \text{ Kg mol}^{-1}$ , see GIWAXS pattern in Figure S19, Supporting Information) we see i) that the enthalpy recovery peak associated to the physical ageing of the glassy regions becomes more pronounced (see Figure 8k) and ii) that the macroscopic flow (liquefaction) occurs at 190 °C, coinciding approximately with the supposed  $T_g$ , as it should be the case for a polymer with a low degree of structural order (Figure 8l). We recall that the solid–liquid transition occurred at almost  $\approx 300$  °C in PBnDT-FTAZ containing a larger fraction of structurally ordered region (Figure 4c), as the liquefaction of this sample results mainly from the melting of the mesophase.
- (d) In good agreement with this interpretation is DMA data shown in Figure 8b, which feature a decrease of  $E'$  and a shoulder in the  $\tan \delta$  curve (identified as  $T_a$ ) in the temperature region where the calorimetric  $T_g$  of the material is observed. These can be associated with the mechanical  $\alpha$ -relaxation of disordered polymer backbones, which is connected to the glass transition.<sup>[25]</sup> It is worth highlighting, moreover, that the stiffness of the material increases at 250 °C, which agrees with the improvement of the overall structural order detected by GIWAXS above  $T_g$ .

Taken together, these observations reinforce our interpretation that the MT state is characterized by the presence of glassy regions of backbones in the materials. Equally importantly, the absence of clear signs of the MT region in polymers like in PBDB-T-Cl (and others shown in Figure 7) suggests a limited influence of glassy domains and that the importance of the  $T_g$  can be minor in these materials. In agreement with this hypothesis, recent studies performed for similar donor–acceptor conjugated polymers with rigid backbones have proposed that the fraction of structurally ordered material is close to 100%.<sup>[7]</sup> Must note that a small fraction of glassy regions likely exists in D18, PBDB-T-2F (PM6), D18-Cl, and PBDB-T-Cl, but similarly to the case of semicrystalline polymers with high degree of crystallinity, e.g., polyethylene and polyethylene oxide, the density of mesophase domains in these materials can be so high that disordered material regions are difficult to detect.

As already mentioned, neat polymers in the MT state undergo minor structural changes because large-scale molecular motions are slow in this temperature region. This is also applicable to polymer domains in BHJ (see Figure S20a, Supporting Information). However, a quick literature search reveals that some of the best performing OSCs employing, e.g., FTAZ,<sup>[36]</sup> D18,<sup>[37]</sup> and PM6<sup>[38]</sup> include a low temperature thermal annealing step (likely in the MT region or the lowest part of the LT region in the case of D18 and PM6). Although they might be aimed at evaporating solvent rests occluded in the BHJ, it is well-known that thermal annealing in the MT region can result in significant changes in the BHF nanomorphology. Even polymers that do not feature observable MT states in the neat state tend to form bicomponent glassy domains when blended with an NFA. The rate at which

such intermixed glassy domains evolve toward a more equilibrated state can be higher than that of neat polymers because now donor:acceptor (im)miscibility comes also into play. Consequently, when intermixed glassy domains are annealed at temperatures within the MT region, immiscibility of donor and acceptor compounds may drive their phase separation, altering the BHF nanomorphology (see Figure S20b, Supporting Information) and likely resulting in the degradation of devices.<sup>[2a,b,39]</sup>

Lastly, the HT state represents the principal state of aggregation of PBnDT-FTAZ between the  $T_g$  and the melting of crystallites, occurring at  $\approx 320$  °C (see Figure 8b). The thermal behavior described above for the HT region is analogous to that observed in “regular” semicrystalline polymers when they are annealed between the  $T_g$  and the  $T_m$ . Therefore, our interpretation of the HT region is also analogous to the accepted interpretation of semicrystalline materials. It can thus be argued that in the HT region, the material is composed of the layered mesophase and supercooled liquid regions. Given that both regions are out of thermodynamic equilibrium, both can evolve toward more equilibrated thermodynamic states. Thus, thermal annealing within the HT region can result in significant structural alterations. The in situ temperature-resolved GIWAXS data (included in Figure 8b) demonstrate that the intensity of the (100) and (010) peaks exhibits a rapid increase as the temperature is elevated above 240 °C (see also Figure S21, Supporting Information). Moreover, Figure 7b reveals that  $\Delta H$  values increase rapidly when these polymers are annealed in the HT region. These results are compatible with the increase of the fraction of mesophase in the materials. Specifically, supercooled liquid regions tend to phase-transform into new mesophase regions (in a process that is analogous to a cold crystallization of semicrystalline polymers). Moreover, the rapid increase of the  $L_c$  of the (100) and (010) peaks (Figure 8b), the emergence of higher-order ( $h00$ ) peaks in 2D-GIWAXS patterns (Figure 8f; Figure S17 Supporting Information), the decrease of the  $g$ -parameter value shown in Figure S17 of the Supporting Information and elsewhere,<sup>[3]</sup> the rise of the  $\eta$ -values (Table S1, Supporting Information), and a notable alteration in the surface topography of the films, as evidenced by the AFM height images (Figure 8i) and their corresponding height histograms (Figure 8j), highlight that the mesophase regions tend to reduce their free energy through reducing the lattice disorder, homogenizing lattice parameters and increasing crystallite size. It is noteworthy that the most dramatic structural changes occur above the annealing temperatures at which the melting peaks of the novel and preexisting mesophase merge in FSC. Upon the merging of these peaks, a single melting peak exhibits a rapid shift to higher temperatures as the annealing temperature is increased. This indicates that larger, more stable mesophase regions are developing, most likely via a process analogous to melt-recrystallization, as observed in semicrystalline polymers. It is regrettable that FSC does not permit the investigation of annealing temperatures above 280 °C due to thermal degradation during the isothermal steps. However, the in situ GIWAXS analysis of PBnDT-FTAZ in the high-temperature-annealing region (shown in Figure 4b) reveals that the ultimate melting temperature for PBnDT-FTAZ is  $\approx 340$  °C.

Thermal annealing donor:acceptor BHJs at temperatures within HT region is expected to induce significant structural and

morphological changes. For example, because donor polymer and typical NFAs often exhibit similar  $T_g$  values<sup>[40]</sup> the HT region is above the  $T_g$  of glassy intermixed domains. Therefore, intermixed regions are expected to undergo a rapid purification during thermal annealing at temperatures of the HT region, likely resulting in a nanomorphology with excessive phase separation. Moreover, typical NFAs will tend to cold-crystallize<sup>[41]</sup> at temperatures above  $T_g$ , which might result in severe alterations of the BJH nanomorphology.

It is important to note that our interpretation of the HT region differs from that of O'Connor and co-workers,<sup>[42]</sup> who interpreted that PBnDT-FTAZ is in a liquid-crystalline state within the specified temperature range. In addition to the experimental results presented above, which can be adequately interpreted on the assumption that PBnDT-FTAZ is composed of a solid-mesophase (including  $\pi$ -stacked backbones and mobile side chains) and a supercooled liquid, Figure S22 of the Supporting Information shows that our PBnDT-FTAZ material is neither a liquid nor birefringent in this temperature region, which are qualities that can be expected for a liquid-crystalline polymer.<sup>[43]</sup> However, it cannot be ruled out that when PBnDT-FTAZ is annealed within the HT region, the supercooled liquid regions evolve to a layered liquid-crystalline phase prior to transform into the solid mesophase, which could explain the elevated degree of lamellar order and alignment they found. Likewise, we cannot rule out either that the presence/absence of a liquid-crystalline phase is due to batch-to-batch variations in, e.g., chemical defects in backbones.

Summarizing all of our observations, Figure 9 shows the general thermotropic phase behavior of benzodithiophene-based polymers, including their aggregate states and the transition temperatures. At high-temperatures, all polymers are in the HT state, which is characterized by the coexistence of the solid mesophase, along with other regions where the material is in a supercooled liquid phase. The upper limit of the HT state is the  $T_m$  of the mesophase. The MT state, which is found in PBnDT-FTAZ and PTQ10, combines amorphous glassy regions with mesophase regions. Therefore, PBnDT-FTAZ and PTQ10 exhibit a measurable  $T_g$ . At low temperatures, within the LT state, side-chain layers within the mesophase are in a glassy state. Thus, side-chain glassy regions also exhibit a  $T_{g,SC}$ . Interestingly, most of the best-performing OSCs are based in polymers featuring two temperature regions (e.g., D18, D18-Cl, PM6, etc.). Consequently, our results might suggest that large amounts of nanoscale mesophase regions (hence low fractions of disordered, glassy material) are beneficial for device performance. We argue that a high density of nanoscopic mesophase domains can aid in creating a suitable BHJ nanomorphology, exhibiting a suitable phase separation length scale and high domain purity.

### 3. Conclusions

The solid aggregate states, microstructure/nanomorphology and thermotropic behavior of a series of benzodithiophene-based polymers that find applications as donor components in high-performing OPV devices were here reported. Our data suggests that these polymers tend to form a solid mesophase that differs from other low-order structures previously identified in polymers, including condensation crystals, hexagonal phases, columnar mesophases, vitrified liquid crystals, (micro)paracrystals, and so

forth. This mesophase seems to be a layered structure in which solid-like layers of  $\pi$ -stacked backbone segments and mobile, liquid-like layers of aliphatic side chains are alternated. Within aromatic layers, backbone chains are parallelly aligned forming a sort of 2D columnar-like structure (i.e., like in paracrystals and condensation crystals). According to GIWAXS, lamellar periodicity extends over at least 3–4 molecular layers in the as-cast films, while  $\pi$ -stacked backbone segments can extend over—at least—seven  $\pi$ -stacked chain segments (e.g., in D18). We note that these values might be larger than those mentioned as the loss of the X-ray coherence results mainly from the disorder of the mesophase lattice. Thus, the structure of the mesophase may resemble a self-assembled stack of nanoscale 2D-platelets whose degree of order exceeds that typically considered as “short-range-order.” From a morphological point of view, this mesophase could be pictured as being an intermediate situation between the “disordered smectic,  $\Sigma_d$ ” and the “ordered smectic,  $\Sigma_o$ ” in Erbert’s classification<sup>[11a,b]</sup> and also exhibit similarities with the solid mesophases named as A-modifications found in aromatic polyesters and polyamides bearing flexible side chains.<sup>[11c,22b,44]</sup> However, differently from these, the order–disorder transition and the solid–liquid transition in benzodithiophene-based polymers occurs approximately at the same temperatures, which is why this mesophase seems different from other mesophases reported. At a larger length scale the solid mesophase tends to form nanoscale fibril-like domains, where polymer backbones align parallelly along the long axis of the fibril. Our data confirm, moreover, that at regular device operation temperatures spun cast films of benzodithiophene-based polymer exhibit a biphasic nanomorphology, i.e., a solid-state microstructure that includes two different aggregate states, namely, the solid mesophase and a structurally disordered, amorphous-like state. However, the fraction of amorphous-like regions in many benzodithiophene-based polymers—including some of the champion polymers for OSCs, namely, D18, D18-Cl, PM6, PBDB-T-Cl, and so on—seems to be minor and these materials do not exhibit a detectable calorimetric  $T_g$ . Nevertheless, we argue that the presence of disordered regions might result in overestimations of the amount of lattice disorder in semiconducting polymers, if the latter is calculated from  $g$ -parameters from 1st order GIWAXS peaks.

Benzodithiophene-based polymers display a markedly different thermotropic behavior contingent on the fraction of mesophase regions. Polymers with high degrees of ordered material, including D18, PBDB-T-2F (PM6), D18-Cl, and PBDB-T-Cl, display two temperature regions with different thermal response in the solid state and two detectable phase transition temperatures. In contrast, polymers such as PBnDT-FTAZ and PTQ10 display three distinct temperature regions and three detectable phase transition temperatures. Because the best performing OSCs are based in polymers featuring two temperature regions (e.g., D18, D18-Cl, PM6, etc.) we hypothesize that high amounts of nanoscale mesophase regions (hence low fractions of disordered, glassy material) are beneficial. A high fraction of nanoscale mesophase can promote a suitable BHJ nanomorphology, exhibiting a suitable phase separation length scale (that reduce exciton recombination) and pure domains (that enhance charge transport). In the high-temperature region, materials are in the so-called HT state, which is present in all semiconducting polymers analyzed. The HT state is distinguished by the co-

existence of a solid mesophase, along with other regions where the material is in a supercooled liquid phase. During thermal annealing at temperatures of the HT state, the supercooled liquid regions tend to phase transform into new mesophase regions (in a process analogous to the cold crystallization of semicrystalline polymers), while the mesophase regions tend to reduce their free energy by reducing lattice disorder, homogenizing lattice parameter and increasing crystallite size. Combining mesophase regions with glassy, amorphous-like regions, a MT state is found in polymers with low fractions of structural order (like PBnDT-FTAZ) and, likely, in polymers with more flexible backbone chains, such as PTQ10. Amorphous regions are glassy and, therefore, PBnDT-FTAZ and PTQ10 exhibit a  $T_g$ . The application of thermal annealing to these polymers within the MT state results in minimal structural alteration, although it does induce the physical aging of glassy domains. Lastly, the LT state, which is also present in all polymers, is formed when the side-chain regions within the mesophase vitrify. The application of thermal annealing to the polymers in the LT state does not result in any discernible structural changes.

## 4. Experimental Section

**Materials:** The polymer donors PBDB-T-2Cl (also known as PBDB-T-2Cl or PM7;  $M_w = 117 \text{ kg mol}^{-1}$ ,  $D = 1.6$ ) and D18 ( $M_w = 63 \text{ kg mol}^{-1}$ ,  $D = 1.9$ ) were supplied by Ossila Ltd. PBnDT-FTAZ ( $M_w = 117 \text{ kg mol}^{-1}$ ,  $D = 2.2$ ), was synthesized as previously reported.<sup>[26]</sup> Chlorobenzene (CB) was purchased from Merck and used as received. The polymers PBDB-T, PBDB-T-2F, and PTQ10 were purchased from Ossila Ltd, while D18-Cl was synthesized as reported by Zhong et al.<sup>[45]</sup>

**Sample Preparation: Nonaligned Thin Films:** Unless indicated, all polymers were spun cast from  $20 \text{ mg mL}^{-1}$  chlorobenzene solutions at 2000 rpm during 60 s.

**Polymer Film Alignment by High Temperature Rubbing:** Polymer films were subjected to a hot rubbing treatment in air to induce the unidirectional alignment of fibrillar mesophase domains. A homemade rubbing apparatus consisting of a linear stage ( $0.2 \text{ mm s}^{-1}$ ) with its temperature set to  $200 \text{ }^\circ\text{C}$  and a rotating cylinder (6 cm in diameter, 750 rpm) covered with a microfiber cloth was employed. The relative position between the cloth and the sample, thus the contact pressure, was adjusted using a micrometric screw. While located atop the linear stage, the samples were thermalized for at least 2 min and the temperature controlled using a software-based proportional-integral-derivative algorithm. The synchronization of the motors and temperature controllers was orchestrated in Python with a Raspberry Pi. Samples were not further annealed after the rubbing process was completed. A photograph of the setup is provided in Figure S4 of the Supporting Information.

**Characterization-Fast Scanning Calorimetry:** FSC measurements were conducted using a Mettler Toledo Flash DSC 1, which is equipped with a two-stage intracooler, thereby enabling temperature control between  $-90$  and  $450 \text{ }^\circ\text{C}$  and nitrogen purge ( $75 \text{ mL min}^{-1} \text{ N}_2$  gas flow). Prior to utilization, the MultiSTAR UFS1 ( $24 \times 24 \times 0.6 \text{ mm}^3$ ) MEMS chip sensors were conditioned and corrected in accordance with the established specifications. In order to conduct the experiments, the polymer solutions were spin-cast onto the reverse side of the chip sensor. The first heating scan of the spin-coated films was analyzed by scanning the samples between  $-90$  and  $450 \text{ }^\circ\text{C}$  at a rate of  $4000 \text{ }^\circ\text{C s}^{-1}$ . Second heating scans were obtained under the same experimental conditions after the film was cooled from  $450$  to  $-90 \text{ }^\circ\text{C}$  at a rate of  $4000 \text{ }^\circ\text{C s}^{-1}$ . Isothermal annealing experiments and step-response experiments were performed on small pieces of materials.

**Grazing Incidence Wide Angle X-Ray Scattering:** GIWAXS measurements were conducted at the BL11 NCD-SWEET beamline at the ALBA Synchrotron Radiation Facility in Spain. The incident X-ray beam energy

was set to  $12.4 \text{ keV}$  using a channel-cut Si (111) monochromator and collimated with an array of Be Compound Refractive Lenses. The X-ray beam angle of incidence,  $\alpha_i$ , was varied between  $0.1^\circ$  and  $0.15^\circ$  in order to ensure surface sensitivity while minimizing the bulk contribution. The scattering patterns were recorded using a Rayonix LX255-HS area detector, which consists of a pixel array of  $1920 \times 5760$  pixels ( $H \times V$ ) with a pixel size of  $44.54 \times 44.54 \text{ } \mu\text{m}^2$  with a binning mode of  $2 \times 2$ . The data are expressed as a function of the scattering vector ( $q$ ), the reciprocal space wavevector, which was calibrated using  $\text{Cr}_2\text{O}_3$  as the standard sample (NIST), resulting in a sample-to-detector distance of  $200.93 \text{ mm}$ . In situ X-ray experiments were conducted at varying temperatures using a Linkam THMS 600 stage, which was adapted for grazing incidence experiments. The heating rate employed was  $20 \text{ }^\circ\text{C min}^{-1}$ , with a temperature differential of  $4 \text{ }^\circ\text{C}$  between frames. The exposure times for the in situ and ex situ experiments were 1 and 5 s, respectively. All measurements were conducted under nitrogen flow to minimize the potential damage to the films. GIWAXS peak fitting was performed using Fityk and pseudo-Voigt functions with a background formed by an exponential decay function and, if needed, a linear function.<sup>[46]</sup>

**Atomic Force Microscopy:** AFM images were taken using a scanning probe microscope (Dimension ICON, Bruker). The measurements were done in tapping mode under ambient conditions. TESPA-V2 probes with a cantilever length  $\approx 125 \text{ } \mu\text{m}$  were operated at  $\approx 320 \text{ kHz}$  resonant frequency. AFM images were collected at scan rate between  $0.7$  to  $1.2 \text{ Hz s}^{-1}$  and  $512$  lines with target amplitude of  $\approx 0.9 \text{ V}$ . The amplitude setpoint was  $\approx 300 \text{ mV}$ . In order to ensure representative measurement of morphology different areas of each sample were scanned. Furthermore, a CSI Instruments Nano-Observer AFM microscope operating with Nano Solution software (version: 1.37.0.405-SA1) was also employed. The images were acquired using intermittent contact (resonant oscillating) mode. The tip employed for the measurements was the APP Nano ACT (tip of  $< 10 \text{ nm}$  radius, resonant frequency of  $\approx 290 \text{ kHz}$ , and spring constant between  $25$  and  $45 \text{ N m}^{-1}$ ). The cantilever presented the following geometrical aspect: length  $\approx 125 \text{ } \mu\text{m}$ , width  $\approx 35 \text{ } \mu\text{m}$ , thickness  $\approx 4 \text{ } \mu\text{m}$ , and a cone length of  $\approx 15 \text{ } \mu\text{m}$ . Quantitative information about the film nanomorphology was obtained from PSD analysis applied to the AFM height-contrast images using the Gwyddion software (version: 2.64.20231122).

**High-Resolution Transmission Electron Microscope (HRTEM):** Images were obtained with a JEOL 2010 electron microscope, operating at  $200 \text{ kV}$ . The sample inspected was a  $30\text{-nm}$ -thick film, spin-coated from a  $20 \text{ mg mL}^{-1}$  solution in *o*-xylene.

**(Polarized) Optical Microscopy:** Optimal microscopy images were acquired in a Zeiss Scope A1 microscope using a Zeiss EC EPIPLAN 10X/0.25 HD objective (10 ms exposure time). Cross-polarized POM images were acquired in transmission, with the incident light polarized perpendicularly with respect to the analyzer while the samples were rotated manually. The brightest POM images were observed when the rubbing direction was set at  $\approx 45^\circ$  with respect to the cross-polarization axis.

**UV-Vis Spectroscopy:** UV-vis spectra were recorded with a Shimadzu UV-2550 spectrometer with a film adapter. Samples were spin cast on glass slides and thermal treatments were performed in a Linkam hot stage under  $\text{N}_2$  atmosphere.

**Polarized UV-Vis Absorption Spectroscopy:** Polarized absorption spectra were acquired using the POM setup with the polarizer at the analyzer position removed and a FLAME-S-UV-VIS (Ocean Optics) spectrometer coupled by optical fiber at the transmitted beam path. To avoid the manual rotation of the sample, blank transmittance spectra ( $I_0$ ) were obtained with the incident polarization set parallel and perpendicular to the rubbing direction. 50 scans of 100 ms (acquisition time) each were collected and averaged to obtain smooth intensity spectra with the sample removed ( $I_0$ ) and the sample in place ( $I$ ). The absorbance ( $A$ ) for each polarization condition was then calculated as  $A = \log_{10}(I_0/I)$ .

**Dynamic Mechanical Analysis:** Measurements were conducted using a Q800 from TA Instruments, from  $-80$  to  $300 \text{ }^\circ\text{C}$  at a frequency of  $1 \text{ Hz}$  and a heating rate of  $3 \text{ }^\circ\text{C min}^{-1}$ . A plain weave glass fiber mesh with a weight of  $25 \text{ gm}^{-2}$  (obtained from Easycomposites), was cut at a  $45^\circ$  angle into pieces of  $4 \text{ cm}$  by  $0.5 \text{ cm}$ . These pieces were drop coated, then dried under vacuum conditions at room temperature.

## Supporting Information

Supporting Information is available from the Wiley Online Library or from the author.

## Acknowledgements

J.M. thanks financial support from the MICIU (Grant Agreement No. PID2021-126243NB-I00), the European Research Council (Grant No. 101086805). J.A. thanks the CIF-UDC for her scholarship. C.M. thanks the Swedish Research Council for financial support (2022-02977). GIWAXS experiments were performed at NCD-SWEET beamline at ALBA Synchrotron with the collaboration of ALBA staff. The authors thank Alberto Peinador for the GIWAXS data of donor:acceptor blends. J.M. is grateful to O.M.V. for many fruitful overnight discussions. The authors acknowledge Universidade da Coruña /CISUG for the funding received for open access charges. H.A. acknowledges support by Goodnight Innovation Distinguished Professor endowment.

## Conflict of Interest

The authors declare no conflict of interest.

## Data Availability Statement

The data that support the findings of this study are available from the corresponding author upon reasonable request.

## Keywords

crystallization, mesophases, organic solar cells, polymer structure, semiconducting polymers

Received: February 9, 2025  
Revised: April 14, 2025  
Published online: May 20, 2025

- [1] R. Noriega, J. Rivnay, K. Vandewal, F. P. V. Koch, N. Stingelin, P. Smith, M. F. Toney, A. Salleo, *Nat. Mater.* **2013**, *12*, 1038.
- [2] a) M. Ghasemi, N. Balar, Z. Peng, H. Hu, Y. Qin, T. Kim, J. J. Rech, M. Bidwell, W. Mask, I. McCulloch, W. You, A. Amassian, C. Risko, B. T. O'Connor, H. Ade, *Nat. Mater.* **2021**, *20*, 525; b) L. Ye, H. Hu, M. Ghasemi, T. Wang, B. A. Collins, J.-H. Kim, K. Jiang, J. H. Carpenter, H. Li, Z. Li, T. McAfee, J. Zhao, X. Chen, J. L. Y. Lai, T. Ma, J.-L. Bredas, H. Yan, H. Ade, *Nat. Mater.* **2018**, *17*, 253; c) Z. Peng, L. Ye, H. Ade, *Mater. Horiz.* **2022**, *9*, 577.
- [3] S. Marina, E. Gutierrez-Fernandez, J. Gutierrez, M. Gobbi, N. Ramos, E. Solano, J. Rech, W. You, L. Hueso, A. Tercjak, H. Ade, J. Martin, *Mater. Horiz.* **2022**, *9*, 1196.
- [4] a) C. Greco, A. Melnyk, K. Kremer, D. Andrienko, K. C. Daoulas, *Macromolecules* **2019**, *52*, 968; b) C. R. Snyder, D. M. DeLongchamp, *Curr. Opin. Solid State Mater. Sci.* **2018**, *22*, 41; c) C. R. Snyder, R. J. Kline, D. M. DeLongchamp, R. C. Nieuwendaal, L. J. Richter, M. Heeney, I. McCulloch, *J. Polym. Sci., Part B: Polym. Phys.* **2015**, *53*, 1641.
- [5] C. Guo, Y. Fu, D. Li, L. Wang, B. Zhou, C. Chen, J. Zhou, Y. Sun, Z. Gan, D. Liu, W. Li, T. Wang, *Adv. Mater.* **2023**, *35*, 2304921.
- [6] a) R. Noruzi, E. Lim, B. S. S. Pokuri, M. L. Chabiny, B. Ganapathysubramanian, *npj Comput. Mater.* **2022**, *8*, 38; b) L. Biniek, N. Leclerc, T. Heiser, R. Bechara, M. Brinkmann, *Macromolecules* **2013**, *46*, 4014; c) C. J. Takacs, N. D. Treat, S. Krämer, Z. Chen, A. Facchetti, M. L. Chabiny, A. J. Heeger, *Nano Lett.* **2013**, *13*, 2522.
- [7] C. Cendra, L. Balhorn, W. Zhang, K. O'Hara, K. Bruening, C. J. Tassone, H.-G. Steinrück, M. Liang, M. F. Toney, I. McCulloch, M. L. Chabiny, A. Salleo, C. J. Takacs, *ACS Macro Lett.* **2021**, *10*, 1306.
- [8] F. Auriemma, C. De Rosa, P. Corradini, in *Interphases and Mesophases in Polymer Crystallization II* (Ed: G. Allegra), Springer, Berlin **2005**, p. 1.
- [9] G. Ungar, *Polymer* **1993**, *34*, 2050.
- [10] a) A. M. Hindeleh, R. Hosemann, *J. Phys. C: Solid State Phys.* **1988**, *21*, 4155; b) A. M. Hindeleh, R. Hosemann, *J. Mater. Sci.* **1991**, *26*, 5127.
- [11] a) E. L. Wood, C. Greco, D. A. Ivanov, K. Kremer, K. C. Daoulas, *J. Phys. Chem. B* **2022**, *126*, 2285; b) M. Ebert, O. Herrmann-Schönherr, J. H. Wendorff, H. Ringsdorf, P. Tschirner, *Liq. Cryst.* **1990**, *7*, 63; c) M. Steuer, M. Hörth, M. Ballauff, *J. Polym. Sci., Part A: Polym. Chem.* **1993**, *31*, 1609; d) D. R. Greer, M. A. Stolberg, S. Xuan, X. Jiang, N. P. Balsara, R. N. Zuckermann, *Macromolecules* **2018**, *51*, 9519.
- [12] a) B. Wunderlich, M. Möller, J. Grebowicz, H. Baur, *Conformational Motion and Disorder in Low and High Molecular Mass Crystals*, Advances in Polymer Science, Vol. 87, Springer Berlin, Heidelberg **1988**; b) B. Wunderlich, *Macromol. Symp.* **1997**, *113*, 51.
- [13] a) J. Watanabe, Y. Takashina, *Macromolecules* **1991**, *24*, 3423; b) G. Ungar, *Mol. Cryst. Liq. Cryst.* **2003**, *396*, 155.
- [14] B. Wunderlich, *J. Appl. Polym. Sci.* **2007**, *105*, 49.
- [15] a) B. Wunderlich, *Macromolecular Physics*, Academic Press, New York **1980**; b) B. Wunderlich, in *Integration of Fundamental Polymer Science and Technology—2* (Eds: P. J. Lemstra, L. A. Kleintjens), Springer Netherlands, Dordrecht **1988**, p. 329; c) B. Wunderlich, *Thermochim. Acta* **1999**, *37*, 340.
- [16] M. Cocca, R. Androsch, M. C. Righetti, M. Malinconico, M. L. Di Lorenzo, *J. Mol. Struct.* **2014**, *1078*, 114.
- [17] a) R. Hosemann, A. M. Hindeleh, *J. Macromol. Sci., Part B: Phys.* **1995**, *34*, 327; b) J. Rivnay, R. Noriega, R. J. Kline, A. Salleo, M. F. Toney, *Phys. Rev. B* **2011**, *85*, 84.
- [18] G. K. Williamson, W. H. Hall, *Acta Metall.* **1953**, *1*, 22.
- [19] B. E. Warren, B. L. Averbach, *J. Appl. Phys.* **1950**, *21*, 595.
- [20] A. M. Hindeleh, S. M. Abdo, *Polymer* **1989**, *30*, 218.
- [21] a) D. T. Duong, V. Ho, Z. Shang, S. Mollinger, S. C. B. Mannsfeld, J. Dacuña, M. F. Toney, R. Segalman, A. Salleo, *Adv. Funct. Mater.* **2014**, *24*, 4515; b) A. Sharma, X. Pan, J. M. Bjuggren, D. Gedefaw, X. Xu, R. Kroon, E. Wang, J. A. Campbell, D. A. Lewis, M. R. Andersson, *Chem. Mater.* **2019**, *31*, 6740.
- [22] a) M. Ballauff, G. F. Schmidt, *Makromol. Chem., Rapid Commun.* **1987**, *8*, 93; b) M. Ballauff, G. F. Schmidt, *Mol. Cryst. Liq. Cryst.* **1987**, *147*, 163.
- [23] M. Panar, P. Avakian, R. C. Blume, K. H. Gardner, T. D. Gierke, H. H. Yang, *J. Polym. Sci., Polym. Phys. Ed.* **1983**, *21*, 1955
- [24] a) S. A. Mollinger, B. A. Krajina, R. Noriega, A. Salleo, A. J. Spakowitz, *ACS Macro Lett.* **2015**, *4*, 708; b) B. T. O'Connor, O. G. Reid, X. Zhang, R. J. Kline, L. J. Richter, D. J. Gundlach, D. M. DeLongchamp, M. F. Toney, N. Kopidakis, G. Rumbles, *Adv. Funct. Mater.* **2014**, *24*, 3422; c) K. Gu, Y.-L. Loo, *J. Polym. Sci., Part B: Polym. Phys.* **2019**, *57*, 1559.
- [25] N. Balar, J. J. Rech, S. Siddika, R. Song, H. M. Schrickx, N. Sheikh, L. Ye, A. M. Bonilla, O. Awartani, H. Ade, W. You, B. T. O'Connor, *Adv. Funct. Mater.* **2022**, *32*, 2105597.
- [26] Q. Zhang, L. Yan, X. Jiao, Z. Peng, S. Liu, J. J. Rech, E. Klump, H. Ade, F. So, W. You, *Chem. Mater.* **2017**, *29*, 5990.
- [27] a) C. Guo, Y. Sun, L. Wang, C. Liu, C. Chen, J. Cheng, W. Xia, Z. Gan, J. Zhou, Z. Chen, J. Zhou, D. Liu, J. Guo, W. Li, T. Wang, *Energy Environ. Sci.* **2024**, *17*, 2492; b) S. Marina, E. Gutierrez-Fernandez, J. Gutierrez, M. Gobbi, N. Ramos, E. Solano, J. Rech, W. You, L. Hueso, A. Tercjak, H. Ade, J. Martin, *Mater. Horiz.* **2022**, *9*, 1196; c) Y. Lin, M. I. Nugraha, Y. Firdaus, A. D. Scaccabarozzi, F. Aniés, A.-H. Ernwas, E. Yengel, X. Zheng, J. Liu, W. Wahyudi, E. Yarali, H. Faber, O. M. Bakr, L. Tsetseris, M. Heeney, T. D. Anthopoulos, *ACS Energy Lett.* **2020**, *5*, 3663; d) O. Amargós-Reyes, J.-L. Maldonado, D. Romero-Borja, D. Barreiro-

- Argüelles, I. Caballero-Quintana, O. Barbosa-García, J. A. Gaspar, J. *Mater. Sci.* **2019**, *54*, 2427.
- [28] J. H. Carpenter, M. Ghasemi, E. Gann, I. Angunawela, S. J. Stuard, J. J. Rech, E. Ritchie, B. T. O'Connor, J. Atkin, W. You, D. M. DeLongchamp, H. Ade, *Adv. Funct. Mater.* **2019**, *29*, 1806977.
- [29] V. Pirela, A. J. Müller, J. Martín, *J. Mater. Chem. C* **2024**, *12*, 4005.
- [30] R. Hosemann, M. P. Hentschel, U. Schmeisser, R. Brückner, *J. Non-Cryst. Solids* **1986**, *83*, 223.
- [31] T. J. Prosa, J. Moulton, A. J. Heeger, M. J. Winokur, *Macromolecules* **1999**, *32*, 4000.
- [32] a) X. Monnier, D. Cavallo, M. C. Righetti, M. L. Di Lorenzo, S. Marina, J. Martin, D. Cangialosi, *Macromolecules* **2020**, *53*, 8741; b) S. Marina, N. P. Kaufmann, A. Karki, E. Gutiérrez-Meza, E. Gutiérrez-Fernández, J. Vollbrecht, E. Solano, B. Walker, J. H. Bannock, J. de Mello, C. Silva, T.-Q. Nguyen, D. Cangialosi, N. Stingelin, J. Martín, *Adv. Mater.* **2020**, *32*, 2005241; c) J. Martín, N. Stingelin, D. Cangialosi, *J. Phys. Chem. Lett.* **2018**, *9*, 990; d) V. Pirela, M. Campoy-Quiles, A. J. Müller, J. Martín, *Chem. Mater.* **2022**, *34*, 10744.
- [33] M. Xiao, A. Sadhanala, M. Abdi-Jalebi, T. H. Thomas, X. Ren, T. Zhang, H. Chen, R. L. Carey, Q. Wang, S. P. Senanayak, C. Jellet, A. Onwubiko, M. Moser, H. Liao, W. Yue, I. McCulloch, M. Nikolka, H. Sirringhaus, *Adv. Funct. Mater.* **2021**, *31*, 2007359.
- [34] D. Cangialosi, A. Alegría, J. Colmenero, *Phys. Rev. E* **2007**, *76*, 011514.
- [35] D. Cangialosi, A. Alegría, J. Colmenero, in *Fast Scanning Calorimetry* (Eds: C. Schick, V. Mathot), Springer International Publishing, Cham **2016**, p. 403.
- [36] Z. Liao, Y. Xie, L. Chen, Y. Tan, S. Huang, Y. An, H. S. Ryu, X. Meng, X. Liao, B. Huang, Q. Xie, H. Y. Woo, Y. Sun, Y. Chen, *Adv. Funct. Mater.* **2019**, *29*, 1808828.
- [37] K. Liu, Y. Jiang, G. Ran, F. Liu, W. Zhang, X. Zhu, *Joule* **2024**, *8*, 835.
- [38] J. Fu, P. W. K. Fong, H. Liu, C.-S. Huang, X. Lu, S. Lu, M. Abdelsamie, T. Kodalle, C. M. Sutter-Fella, Y. Yang, G. Li, *Nat. Commun.* **2023**, *14*, 1760.
- [39] M. Ghasemi, H. Hu, Z. Peng, J. J. Rech, I. Angunawela, J. H. Carpenter, S. J. Stuard, A. Wadsworth, I. McCulloch, W. You, H. Ade, *Joule* **2019**, *3*, 1328.
- [40] E. Mazzolini, Z. Qiao, J. Muller, F. Furlan, M. Sanviti, D. Nodari, M. Rimmele, A. Collauto, C. Deibel, M. Heeney, J. Martin, F. Eisner, J. Nelson, N. Gasparini, J. Panidi, *Adv. Energy Mater.* **2025**, <https://doi.org/10.1002/aenm.202405635>.
- [41] a) S. Marina, A. D. Scaccabarozzi, E. Gutierrez-Fernandez, E. Solano, A. Khirbat, L. Ciammaruchi, A. Iturrospe, A. Balzer, L. Yu, E. Gabirondo, X. Monnier, H. Sardon, T. D. Anthopoulos, M. Caironi, M. Campoy-Quiles, C. Müller, D. Cangialosi, N. Stingelin, J. Martin, *Adv. Funct. Mater.* **2021**, *31*, 2103784; b) E. Gutierrez-Fernandez, A. D. Scaccabarozzi, A. Basu, E. Solano, T. D. Anthopoulos, J. Martín, *Adv. Sci.* **2022**, *9*, 2104977.
- [42] H. M. Schrickx, S. Kashani, L. Buck, K. Ding, J. J. Rech, L. Q. Flagg, R. Li, M. W. Kudenov, W. You, L. J. Richter, H. Ade, B. T. O'Connor, *Adv. Funct. Mater.* **2024**, *34*, 2315183.
- [43] J. Martin, E. C. Davidson, C. Greco, W. Xu, J. H. Bannock, A. Agirre, J. de Mello, R. A. Segalman, N. Stingelin, K. C. Daoulas, *Chem. Mater.* **2018**, *30*, 748.
- [44] S. B. Damman, F. P. M. Mercx, C. M. Kootwijk-Damman, *Polymer* **1993**, *34*, 1891.
- [45] X. Zhong, T.-W. Chen, L. Yan, W. You, *ACS Appl. Polym. Mater.* **2023**, *5*, 1937.
- [46] M. Wojdyr, *J. Appl. Crystallogr.* **2010**, *43*, 1126.